Dispersion control in deformable microchannels

by
Garam Lee
Sc.M., Brown University

Thesis submitted in partial fulfillment of the requirements
for the Degree of Master of Science
in the School of Engineering at Brown University

PROVIDENCE, RHODE ISLAND

May 2020

Signature Page

This thesis by Garam Lee is accepted in its present form by the School of Engineering as satisfying the thesis requirements for the degree of Master of Science.

Date: ______________ ________________________
Daniel M. Harris, Ph.D., Advisor

Approved by the Graduate Council

Date: ______________ ________________________
Andrew G. Campbell, Dean of the Graduate School

Abstract

In fully-developed pressure-driven flow, the spreading of a dissolved solute is enhanced in the flow direction due to transverse velocity variations in a phenomenon now commonly referred to as Taylor dispersion. It is well understood that the characteristics of the dispersion are sensitive to the channel's cross-sectional geometry. Here we demonstrate a method for manipulation of dispersion in a single microchannel via controlled deformation of one side of the channel's walls. Using a rapid-prototyped multi-layer microchip, the lower channel wall is deformed by an external pressure source allowing us to characterize the dependence of the dispersion on the deflection of the channel wall and overall channel aspect ratio. Our experimental measurements are compared directly with theoretical predictions.

Acknowledgments

My deep gratitude goes first to my advisor, Professor Dan Harris, who guided through my graduate education and shared his extensive knowledge with unrelenting support. His endless encouragement and patient allow me to take my first step in this new world successfully. Nothing can pay off the time and effort Dan dedicated to me taking all of my unpolished questions and concerns seriously regardless of its importance and meaningfulness.

I also wish to thank all of the Harris lab members for making a less competitive, but more supportive environment. Especially thanks to Jesse Remeis, for gladly helping me familiarized to the experiment and data analysis when I started this project, and Abigail Taylor for setting up the early stage of Taylor dispersion experiment in the lab and kindly sharing all of techniques and tricks she had developed with great care. I would also like to thank Ajay Harishankar Kumar, helping me with getting intuition in the theoretical background of the project.

I am also indebted to my great friends Dhananjay Bhaskar and Huicong Jiang. Their moral support enabled me to go through hard times when I struggled with experiments and results late at night. On top of that, they always gave me inspiration with their hard work as well. They played an undoubtedly significant role in protecting me against falling into depression. I would like to pay my special regards to Kyuhwe Kang, whose endless words of encouragement, as well as constructive criticism, made me survive through my Master's period.

Lastly, I would like to express my deepest appreciation to my family for their love and continuous care.

Contents

List of Figures

List of Tables

1 Introduction

In fully-developed pressure-driven flow, a dissolved solute exhibits enhanced spreading in the flow direction compared to solely molecular diffusion due to transverse velocity variations [3]. This phenomenon is now commonly referred to as Taylor dispersion.

Such dispersion plays an important role in microfluidic devices. Depending on the application, it affects the functionality of microfluidic devices in a positive (e.g. mixing devices) or a negative way (e.g. separation devices) [4]. Indeed, optimization and control of such effect is often of critical importance when designing a new device.

For pressure-driven flow between two parallel plates, the enhanced dispersion along the flow direction can be described by a 'Taylor-Aris' dispersivity K as

$$\frac{K}{\kappa} = 1 + \frac{1}{210}\left(\frac{Ud}{\kappa}\right)^2 = 1 + \frac{1}{210}Pe^2 \tag{1}$$

where κ is the molecular diffusivity of a solute, U is the average flow velocity, and d is a separation between two parallel plates. The Peclet number Pe is defined as $Pe = Ud/\kappa$ and represents a ratio of diffusive to advective time scales [5].

While Equation (1) serves as a quantification of the dispersivity between two parallel plates, the exact cross-sectional geometry of the channel can significantly affect the proportionality constant. This effect can be captured by introducing a parameter f referred to as the dispersion factor [6] shown as

$$\frac{K}{\kappa} = 1 + \frac{1}{210}\left(\frac{Ud}{\kappa}\right)^2 f = 1 + \frac{1}{210}Pe^2 f \tag{2}$$

Here, d denotes a characteristic channel height. The change of f in a rectangular channel as a function of channel aspect ratio is depicted in Figure 1 as an example.

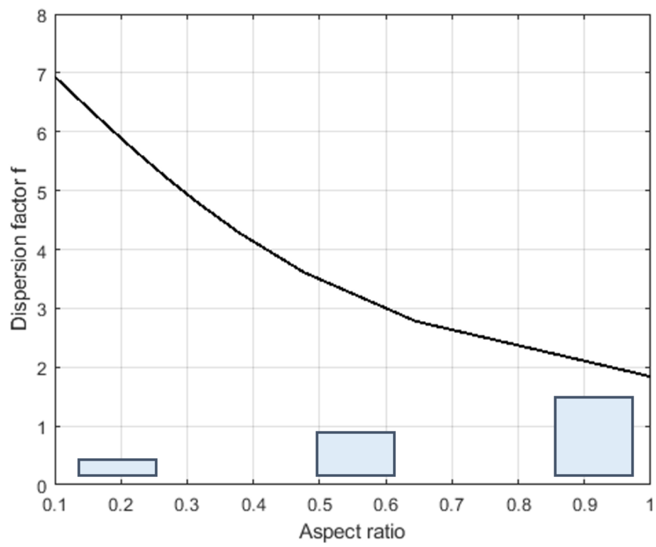

Figure 1: Dispersion factor f of a rectangular channel

The effect of channel geometry on the dispersivity has been extensively studied theoretically [6, 7, 8, 9, 10] and experimentally [4, 11]. However, controlling dispersion in a single channel is previously unexplored since it is challenging to change the channel cross-section once the channel is fabricated. Within this thesis, we demonstrate a novel method to actively manipulate the dispersion properties in a single microchannel via controlled deformation of one side of the channel's walls.

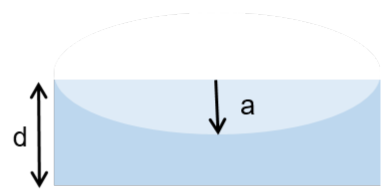

Figure 2: Deformation on one side of the channel's walls

The deflection parameter δ is defined as the ratio of the maximum deformation over the original channel height d as

$$\delta = a/d$$

Positive δ represents the outward deformation, and negative δ represents the inward deformation.

2 Theoretical Background

The dispersion factor f can be mathematically derived using various methods [3, 12, 13]. Following the summary provided in the Dutta et al. review paper [7], the problem reduces to a sequence of two 2D Poisson equations. For an arbitrary channel shape with the cross-section D^* and its boundary ∂D^* scaled with the narrower channel dimension d, the dispersion factor f can be derived as below.

The first Poisson equation is the equation governing the velocity profile with no-slip boundary condition given by

$$\nabla^{*2} u^* = -1 \quad \text{with} \quad u^*\big|_{\partial D^*} = 0 \tag{3}$$

where u^* is the dimensionless velocity scaled as

$$u^* = u / \left(-\frac{d^2}{\mu} \frac{\Delta P}{L} \right)$$

Here, $\Delta P/L$ denotes the pressure drop per unit length in the channel direction and μ indicates the dynamic viscosity of the fluid. The dimensionless average flow velocity U^* is obtained by integrating it over the channel cross-section area as

$$U^* = \frac{1}{A^*} \int_{D^*} u^* \, dA^* \tag{4}$$

where dimensionless cross-section A^* is scaled with d^2. The first moment of the concentration distribution g in the channel direction can be derived using the spatial deviation from the average velocity as a forcing term as

$$\nabla^{*2} g = 1 - \frac{u^*}{U^*} \quad with \quad \nabla^* g \cdot n\big|_{\partial D^*} = 0 \quad and \quad \int_{D^*} g \, dA^* = 0 \tag{5}$$

The dispersion factor f can be obtained from the area integral of the Equation (5) as

$$f = \frac{210}{A^*} \int_{D^*} \frac{u^*}{U^*} g \, dA^* \tag{6}$$

This derivation is formally valid in the long-time regime

$$t \gg \frac{1}{4\pi^2}\frac{W^2}{\kappa} \tag{7}$$

where W is the wider dimension of the cross-section. Dutta and Leighton [6] have numerically shown that the dispersivity K so thus the dispersion factor f approaches 95% of its asymptotic value for

$$t \sim \frac{1}{20}\frac{W^2}{\kappa} \tag{8}$$

in rectangular channels. This timescale estimate is used in designing the experiment setup detailed in this thesis.

In this long time regime, the one-dimensional concentration profile becomes a simple Gaussian centered at a location $x = Ut$ [4] as

$$c(x,t) = \frac{1}{\sqrt{4\pi Kt}}\exp\left(\frac{(x-Ut)^2}{4Kt}\right) \tag{9}$$

At a given position $x_0 = Ut_{max}$ which will serve as a measuring point in the experiment, the concentration versus time becomes

$$c(x_0,t) = \frac{1}{\sqrt{4\pi Kt}}\exp\left(\frac{(x_0-Ut)^2}{4Kt}\right) \tag{10}$$

Here, t_{max} is the time when the intensity reaches its maximum at the given position x_0 and can be obtained by solving

$$\frac{\partial c}{\partial t}(x = x_0, t = t_{max}) = 0. \tag{11}$$

The theoretical value of the dispersion factor f numerically calculated from Equation (6) and the value obtained from experiments with Equation (1) and Equation (10) will be compared. This system of PDEs can be readily solved in numerical packages such as MATLAB or COMSOL. For calculating the theoretical value of f in this thesis, the channel shape without deformation is assumed to be a rectangle of certain aspect ratio, and the top wall is assumed to be deformed in parabolic shape.

3 Microchip fabrication for Taylor dispersion experiment

3.1 Introduction to microchip fabrication technique

In the field of microfluidics, the most commonly used technique to fabricate a microchannel is soft lithography. Soft lithography uses a PDMS layer made by pouring uncured PDMS mixture on a patterned mold on a wafer made by a lithography technique, and cure the PDMS to cast the channel geometry on the PDMS layer. The cured layer is peeled off from the wafer and bonded on a substrate using plasma cleaning. Despite the wide applications and advantages of this technique, the required expensive equipment, highly trained personnel, and a cleanroom environment can be cumbersome for researchers without access to these resources.

Another method to fabricate a microchannel without relying on soft lithography involves laser cutting a spin-coated thin layer of PDMS and bond additional PDMS layers to the top and bottom to form a closed channel [14]. Aside from potential issues with roughness along the internal channel walls due to irregular burns and melting, this process also requires more specialized equipment and trained personnel [15].

Within this thesis, a fabrication method using a desktop craft cutter that is widely accessible and affordable is used. In this technique, double-sided tape is cut into the designed channel shape by a craft cutter and adhered to a transparent film and an acrylic sheet as an upper and lower boundary of the channel. Using a craft cutter for microchannel fabrication has been proposed before [16]; however, the lack of the necessary wall smoothness for many microfluidic experiments have limited the implementation of the technique. Recent work [15] demonstrated an optimized fabrication technique which achieved a surface roughness comparable to other leading fabrication techniques. Ease of use of the devices and extremely short fabrication time makes exploration between different channel design less challenging.

For Taylor dispersion experiments, a channel with a much longer length than typical microchannel sizes is required to reach the asymptotic regime as discussed in Chapter 2. With the craft cutter used in this work, we were able to cut a straight channel with the length up to 20 cm, which is typically limited to 10 cm in soft lithography due to the wafer size. To get around this limitation, previous work in this area have used serpentine channels [4], however the curved portions of such a channel adds additional flow and mixing physics making controlled experiments more challenging.

3.2 Microchip design

3.2.1 Double-layer parallel channel

Multi-layer soft lithography, which was first introduced by S.R. Quake, is a technique to build an active microfluidic system containing microvalves and pumps [17]. The system made from this technique consists of a flow channel and an air channel placed perpendicular to each other. Two channels are separated by a thin PDMS membrane. When pressurized air is applied in the air channel, the membrane is deflected and obstructs the flow in the flow channel.

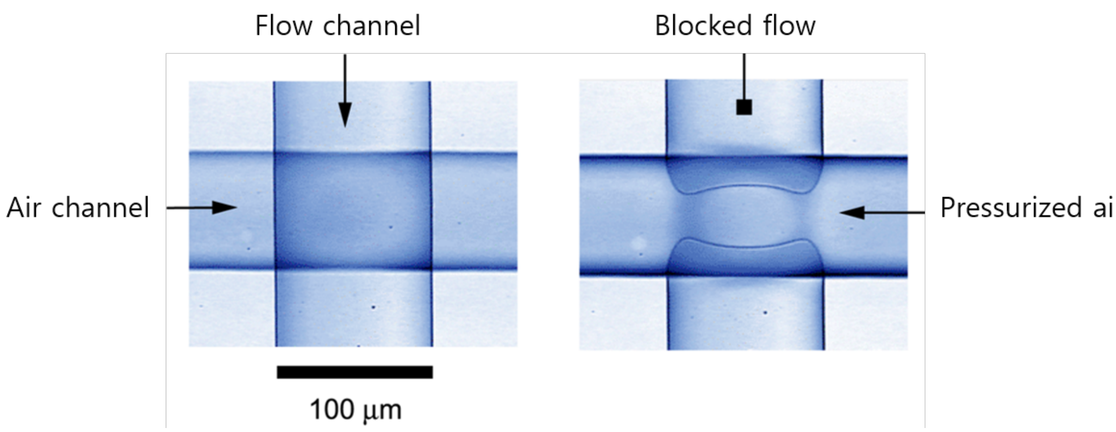

Figure 3: Photograph of a Quake-style valve. Image adopted from [1].

The microvalve design using this technique is often referred to as a Quake-style valve.

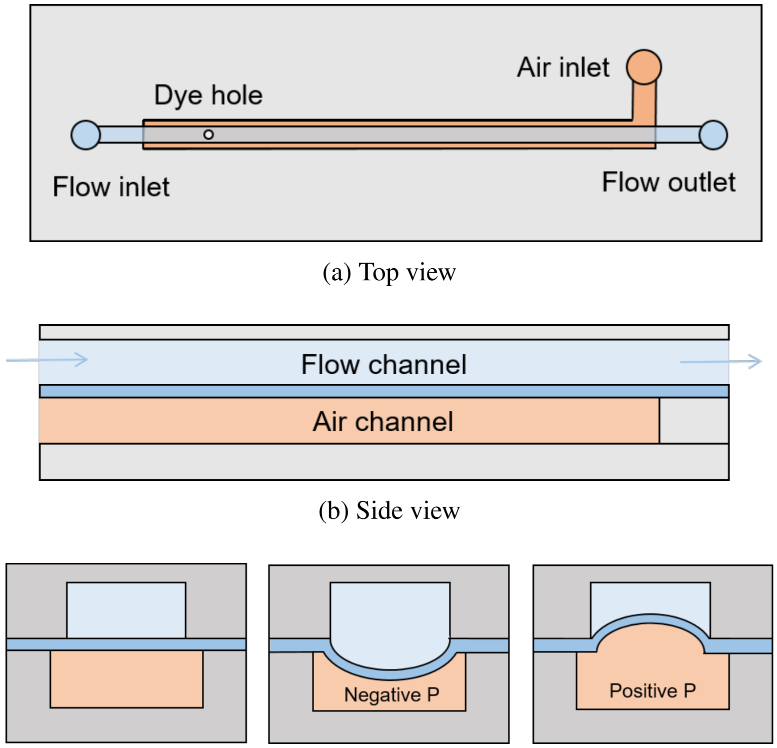

(a) Top view

(b) Side view

(c) Cross-sectional view

Figure 4: Microchip design

Inspired by this multi-layer soft lithography technique, a novel design of double-layer parallel channels is presented within this thesis. Instead of placing the air channel and the flow channel perpendicular to each other, the channels are designed to be aligned parallel. This parallel placement of two channels allows controlling the cross-sectional channel geometry of the entire flow channel by deforming one side of the channel's wall as depicted in Figure 22. The flow channel and the air channel are separated by a flexible membrane so that the membrane can bulge upward and downward by adjusting the pressure in the air channel.

Figure 5: Overall chip structure

Multi-layer soft lithography relies on plasma cleaning or partial curing as a bonding method enabled by the monolithic property of the PDMS layers. In an ideal case, the strength of the interface between layers equals the strength of the bulk elastomer PDMS [17]. However, the quality of these bonding methods is highly susceptible to surface contamination. This aspect makes it challenging to achieve uniform bonding even in a controlled environment, such as a cleanroom. On the contrary, the use of a double-sided tape whose bonding result is less sensitive to surface contamination reduces the risk of failure in bonding between the layers.

		1:5 aspect ratio chip	1:7.5 aspect ratio chip
Flow channel	Width	500 um	750 um
	Length	18 cm	18 cm
	Height	101.6 μm	101.6 μm
Air channel	Width	800 μm	1100 μm
	Length	17 cm	17 cm
	Height	101.6 μm	101.6 μm

Table 1: Channel dimensions

Double-sided polyimide tape (Bertech PPTDE-1) is used as the flow layer and the air layer base material in this work. This tape of the total thickness 101.6um is made of 25.4 um polyimide film with 38.1 um of silicone adhesive coating on each side. For two different aspect ratio chips that are studied, the channels are designed to have dimensions as Table 1. With a mean flow velocity of 1 mm/s in these chips, the corresponding Peclet number *Pe* is calculated as 160.4.

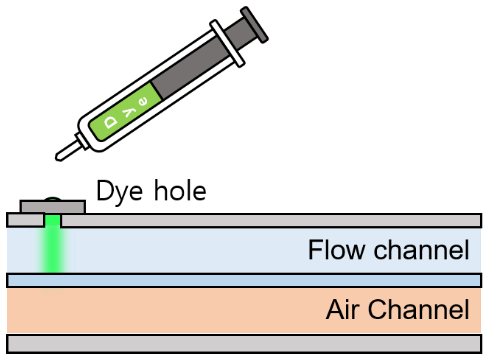

Figure 6: Dye solution introduction method

A small hole for the initial solute introduction is made on the top layer. This hole serves as an inlet allowing the direct access to the flow channel, and sealed with tape at all times except during the solute introduction process.

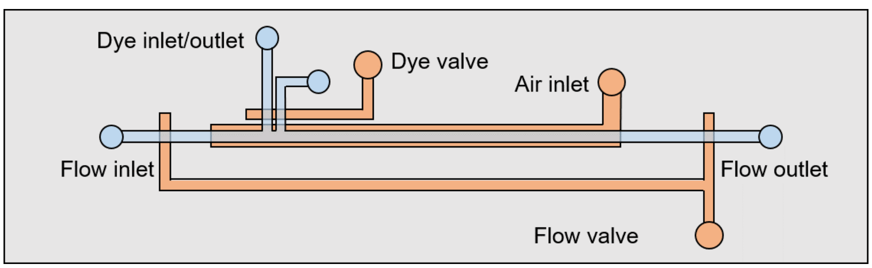

Figure 7: Chip design with valves

The double-layer structure of the chip enables us to build a valve system on the microchip design using the Quake-style valve concept. We were able to implement a dye solution introduction method with such valves by adding a few more components on our chip design as shown in Figure 7. While we were able to fabricate a chip with the design with valves using the craft cutter, the valve system could not block the flow to prevent excessive dye solution to be introduced to the flow channel.

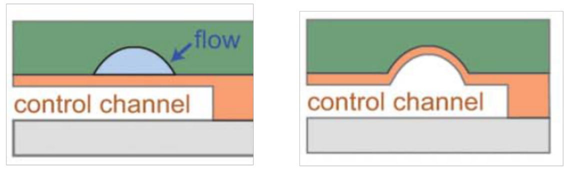

(a) Full valve

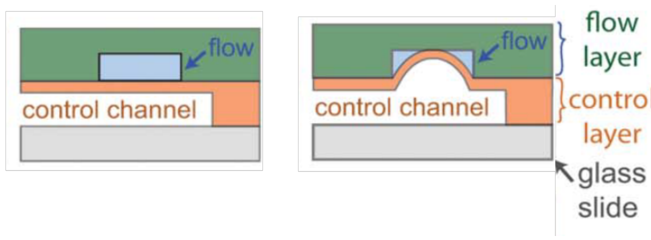

(b) Sieve valve

Figure 8: Schematics of pneumatic valves. Image adopted from [2]

The limitation arises from the rectangular channel geometry. For the valve to function as a full valve to completely block the flow, the channel geometry has to be round so that the membrane can be stretched towards the upper channel wall without having any leakage in the corners. Since the channel fabricated with the proposed method inevitably consists of sharp corners in the flow channel, the valves function as sieve valves which are often used for bead trapping but not suitable for blocking the flow. With this design, we may had have more control over the initial solute distribution. However, we observed that the experimental results are largely insensitive to minor variations to the details of the initial dye patch we achieved with the simpler direct dye introduction method.

3.2.2 Design for different aspect ratios

The relationship between the applied pressure and the maximum deformation of the membrane should be considered carefully in designing a microchip with different aspect ratios or scales. The limitation arises from the mechanical properties of the membrane, and the range of the pressure we can apply using the current setup.

The elastic limit of the membrane restricts the deflection parameter δ we can achieve from a given channel dimension without compromising the repeatability. With the same height, the membrane of a narrow channel design experiences higher strain to obtain the same δ. While it seems narrower channels might have more restrictions regarding the elastic limit compared to wider channels, a more profound problem with narrower channels is that the required pressure to deform to the same δ is significantly higher than wider channels. Thus, with the limitation in the working pressure range, we cannot even stretch the membrane to its elastic limit.

The dispersion factor f depends on the cross-section shape only, and not the physical length scale itself (assuming fully-developed laminar flow). For this reason, the limitation in the pressure range can be overcome by geometrically scaling up the design while keeping the two main parameters fixed: the overall aspect ratio and the deflection parameter δ.

Assuming that the membrane is long enough compared to the width, the axial deformation can be estimated with one-dimensional Euler-Bernoulli model which describes the beam deformation under pressure. With doubly clamped boundary conditions, the beam deformation can be obtained as

$$\frac{d^2}{dx^2}\left(EI\frac{d^2w}{dx^2}\right) = q \quad \text{with} \quad \frac{dw}{dx} = w = 0 \quad \text{at} \quad x = 0, L \tag{12}$$

where $w(x)$ denotes the deflection of the beam in the z-direction and q is the force per unit length uniformly distributed on the beam. L is the length of the beam, E is the elastic modulus, and I is the second moment of area. Solving this equation provides the maximum deformation d_{max} as

$$d_{max} = \frac{qL^4}{384EI} \tag{13}$$

From the Equation 13, the required loads to deflect the beam to the same δ can be compared for different aspect ratios and different scales.

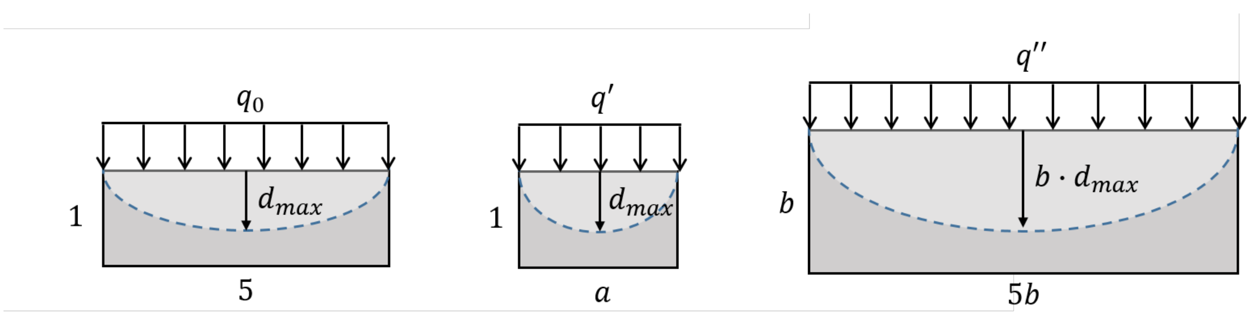

Figure 9: Deflection model with different aspect ratio and scale

For different aspect ratio, the relationship becomes

$$\delta = \frac{d_{max}}{1} = \frac{q_0 \cdot 5^4}{384EI} = \frac{q' \cdot a^4}{384EI}$$

$$q' = \left(\frac{5}{a}\right)^4 q_0 \tag{14}$$

where The symbol q_0 is used to represent the load required to deflect the beam of $L = 5$ to get the maximum deflection of d_{max} as a reference. For different scale, the result becomes

$$\delta = \frac{d_{max}}{1} = \frac{q_0 \cdot 5^4}{384EI} = \frac{b \cdot d_{max}}{d_{max}} = \frac{q'' \cdot 5^4}{384EI}$$

$$q'' = \left(\frac{1}{b}\right)^3 q_0 \tag{15}$$

Assuming that this deflection happens in infinitely long two-dimensional sheet and the calculation is based on the transverse cross-section of the sheet, we can safely expand the approach to two-dimensional model by simply substituting the distributed load q[N/m] with pressure P[N/m^2]. Accordingly, q_0 is substituted by P_0 as well. By doing that with combining Equation 14 and Equation 15, the pressure P required for the design with an arbitrary aspect ratio $1 : a$ scaled with b compared to $1 : 5$ aspect ratio with $\times 1$ scale can be obtained as

$$P = \left(\frac{5}{a}\right)^4 \frac{1}{b^3} P_0 \tag{16}$$

	Aspect ratio			
Scale (layer)	1 : 1	1 : 2	1 : 5	1 : 8
$\times 1$	625.000	39.063	1.000	0.153
$\times 2$	78.125	4.883	0.125	0.019
$\times 3$	23.148	1.447	0.037	0.006
$\times 4$	9.766	0.610	0.016	0.002
$\times 5$	5.000	0.313	0.008	0.001
$\times 6$	2.894	0.181	0.005	0.001

Table 2: Pressure required to deform a membrane to the same δ

Table 2 shows examples of the relative pressure required for different design calculated by Equation 16. In the table, one can notice that the required pressure is drastically increased in a lower aspect ratio design. Even within the elastic limit, the combining effect of the strain and the high pressure difference across the membrane can result in air and water penetration. We observed air penetration through a membrane with a pressure higher than 200 kPa. Hence, an extreme pressure difference between the two channels is unfavorable for the reliability of the test result.

Membrane deformations near the start and the end of the channel will be discussed in the following section.

3.3 Membrane deformation

3.3.1 Material selection

For repeatability of experiments, it is crucial to choose a material for a membrane that can accommodate the working range of strain within their elastic limit. Among a few materials available, plasticized PVC, which is commonly used as food wrap, shows the material properties most suitable for our application [18]. By considering the uniformity, flatness, and the transparency of the material, 'Stretch-tite' premium plastic food wrap has been chosen for this thesis.

While the typical range of the mechanical properties of plasticized PVC is known, the exact value depends on the ratio of plasticizer and PVC. The effect of the plasticizer ratio on their mechanical properties is not extensively documented. Furthermore, the compositions of commercial food wraps are not publicly accessible and are subject to change without notice. Thus, it is necessary to test the mechanical properties of the chosen material as needed.

3.3.2 The geometry of the deformed membrane

Under uniform pressure, an infinitely long membrane is deformed to have a uniform cross-section which can be estimated by a one-dimensional model. In practice, however, a membrane with finite length shows a different deformed shape near the start and the end of the membrane length. From plate bending theory, the transverse displacement w of the membrane with flexural rigidity D subject to a uniform downward pressure P can be modeled as

$$D\left(\frac{\partial^4 w}{\partial x^4}+2\frac{\partial^4 w}{\partial x^2 \partial y^2}+\frac{\partial^4 w}{\partial y^4}\right)=-P \tag{17}$$
$$\frac{\partial w}{\partial x}=w=0 \quad at \quad x=0,L$$
$$\frac{\partial w}{\partial y}=w=0 \quad at \quad y=0,L$$

The partial differential equation is numerically solved using finite difference method in Python. The corresponding code can be found in Appendix A.2.

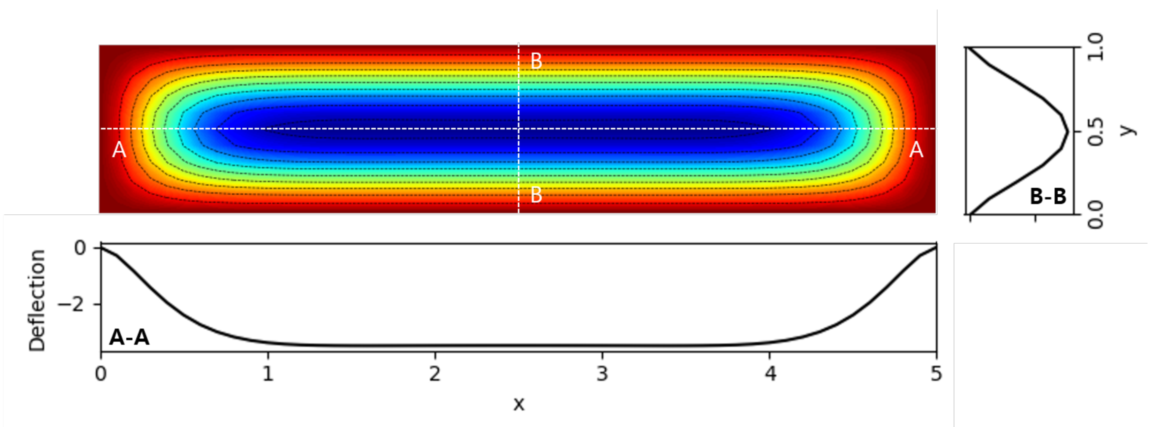

Figure 10: Numerical prediction of the deformed membrane without pretension $D=0.01$,$P=1$

The deformation contour of a rectangular membrane with an aspect ratio of 1 : 5 under uniform pressure is shown in Figure 10. Cross-sectional deformation shapes on the centerlines are depicted in the graphs. Unlike on a square membrane, the region between 1 and 4 in x-direction shows uniform cross-section which we henceforth refer to as the ‘flat region’. This flat region allows us to realize the experiment in a channel with a uniform cross-section to characterize the dispersion behavior for different degrees of deformation.

If the membrane is overly deformed by a given pressure, it becomes hard to achieve precise control over the deformation. In this case, applying pretension on the membrane before adhering to channels can alleviate the problem.

$$-\left(T_x\frac{\partial^2 w}{\partial x^2}+T_y\frac{\partial^2 w}{\partial y^2}\right)+D\left(\frac{\partial^4 w}{\partial x^4}+2\frac{\partial^4 w}{\partial x^2\partial y^2}+\frac{\partial^4 w}{\partial y^4}\right)=-P \tag{18}$$

$$\frac{\partial w}{\partial x}=w=0 \quad at \quad x=0,L$$

$$\frac{\partial w}{\partial y}=w=0 \quad at \quad y=0,L$$

The deformation shape of a pre-tensioned membrane under pressure can be estimated as Equation 3.3.2. Below are the deformation contour of a rectangular membrane with an aspect ratio of 1:5 under different pretension.

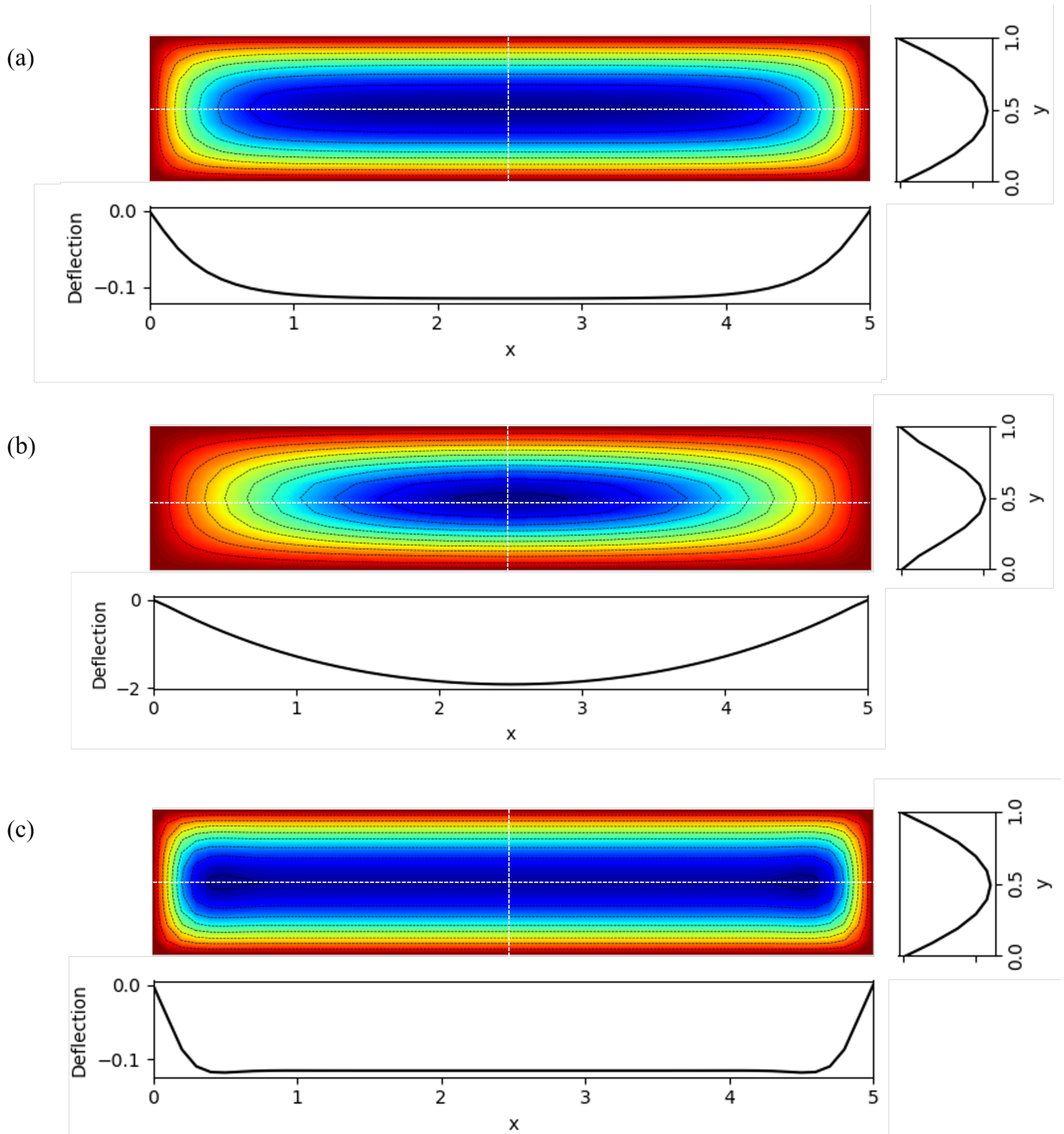

Figure 11: Numerical prediction of the deformed membrane. $D = 0.01, P = -1$
(a) $T_x = 1, T_y = 1$, (b) $T_x = 0, T_y = 1$, (c) $T_x = 1, T_y = 0$

When the pretension is applied on both x and y direction as Figure 11 (a), the deformation is scaled down to the order of 10. However, applying pretension in both directions requires a more complicated setup compared to the pretension in one direction.

Applying significant pretension along the x-axis as shown in Figure11 (b) makes the second order terms of the Equation 3.3.2 dominant resulting in a cross-section deformation along the x-axis that has more of a parabolic shape. For the application in this thesis, this result is undesirable as we obtain to obtain the longest possible flat region along the x-axis.

Pretension along the y-axis allows to reduce the membrane deformation under the pressure as shown in Figure 11 (c). In addition, the flat region becomes longer in this case, which is desirable for our dispersion experiments.

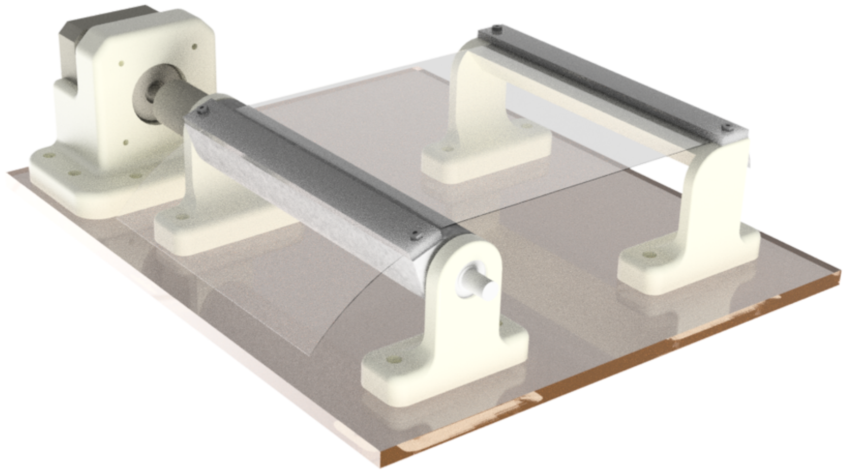

Figure 12: Membrane stretcher

In practice, pretension can be applied to the membrane by a stretcher designed as shown in Figure 12. When the pre-tensioned membrane is attached to the flow layer tape, the adhesive on the tape places a role to hold the pretension.

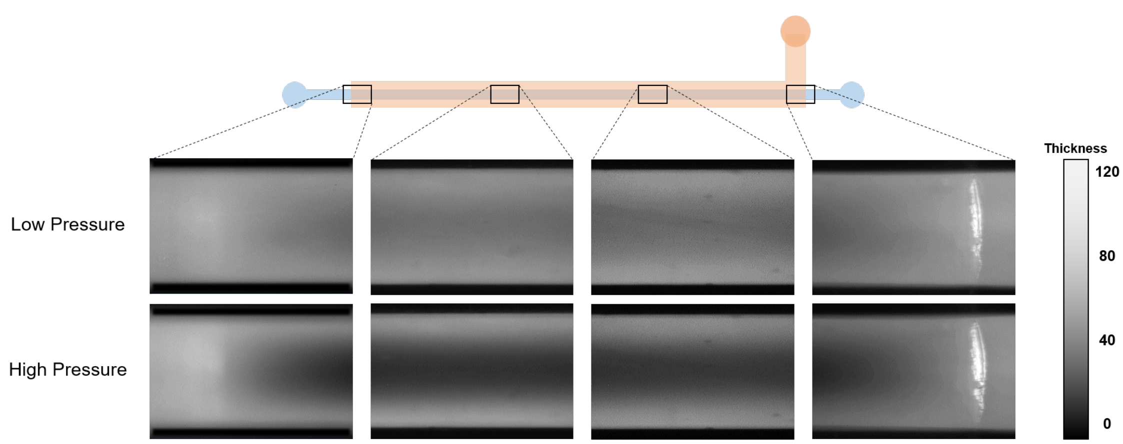

Figure 13: Deformed membrane profile

To visualize the deformed membrane under pressure in the air channel, the flow channel is filled with fluorescein solution and illuminated by a mercury lamp coupled with a blue light filter of excitation wavelength 480 nm. The darker color shows a lack of fluorescein dye molecule along the light path, which represents the upward bulging of the membrane towards the flow channel. As expected, the cross-sectional deformation profiles remain the same in the flat region. With higher pressure applied on the air channel, the membrane deformed more towards the flow channel's upper wall, which yields a darker color on the centerline. A different method of imaging is used for measuring the deformed channel shape to analyze the test result which will be discussed in Chapter 4.1. From measuring the deformed membrane shape, we were able to isolate the flat region as predicted from the numerical calculation. In this thesis, the entire experiment is conducted in the flat region of 15 cm length, 1 cm away from the ends of the membrane.

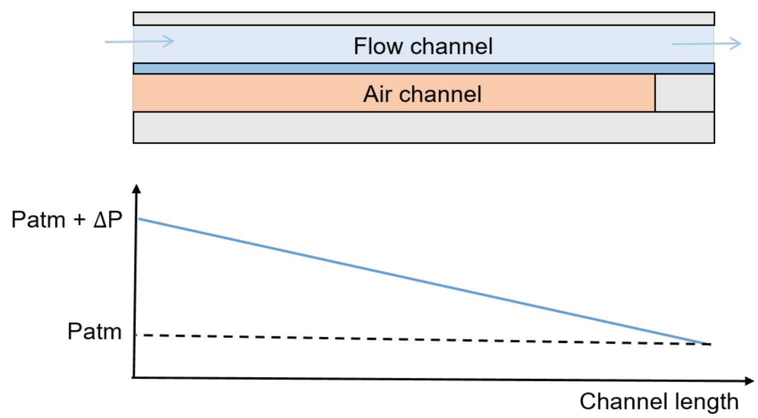

Figure 14: Pressure difference induced by flow

In addition to the uniform pressure from the air channel, the fluid movement in the flow channel also generates pressure difference along the channel length because of the viscosity. In this experiment, however, the pressure applied from the flow channel to the membrane can be neglected since the typical pressure applied from the air channel is in the order of 10 kPa where the pressure drop is in the order of 0.1 kPa for flow velocities of 1 mm/s as used in this thesis.

3.4 Craft-cutter based microchip fabrication

For the top transparency, 0.1mm thick PET film (Grafix Dura-Lar Clear Acetate Alternative) is cut into the chip size with four holes; two holes are for the flow channel, one is for the air channel, and the last one is for the dye hole. A laser cutter (Universal Laser Systems 4.60 with 30 Watt laser) is used to cut the PET film with settings: Power=20, Speed=70, PPI=500, z-axis=-2.4 mm. 3 mm thick acrylic sheet is used for the base and also cut into the chip size using a laser cutter.

To construct the channel's side wall, 1" wide double-sided polyimide tape (Bertech PPTDE-1) is cut by a craft cutter (Silhouette Cameo 3) to the desired channel design. Cutting parameters are set as Razor=4, Force=8, Speed=1, Passes=1. The top transparency and the acrylic base are prepared before cutting the tape to minimize surface contamination on the sticky side of the tape.

The razor blade on the craft cutter passively rotates to its cutting direction by the friction between the cutting material and the razor. Therefore, for sharper corners on the channel design, special care is required for the razor to cut the geometry in an optimal direction [15]. In addition to sharp corners, any changes in the razor direction during the cutting process can yield a discrepancy between the original design and the cutting result. Furthermore, sudden changes in the razor direction can also damage the tape affecting the cutting quality. It is important to avoid such an effect, especially for the flow channel, where it is crucial to obtain a uniform channel width.

The issues with a rotating razor can be minimized by avoiding the use of curves and edges in the design, and changing the cutting order. Cutting orders can be specified in the "Silhouette Studio Design" software by assigning different colors for each group of line segments.

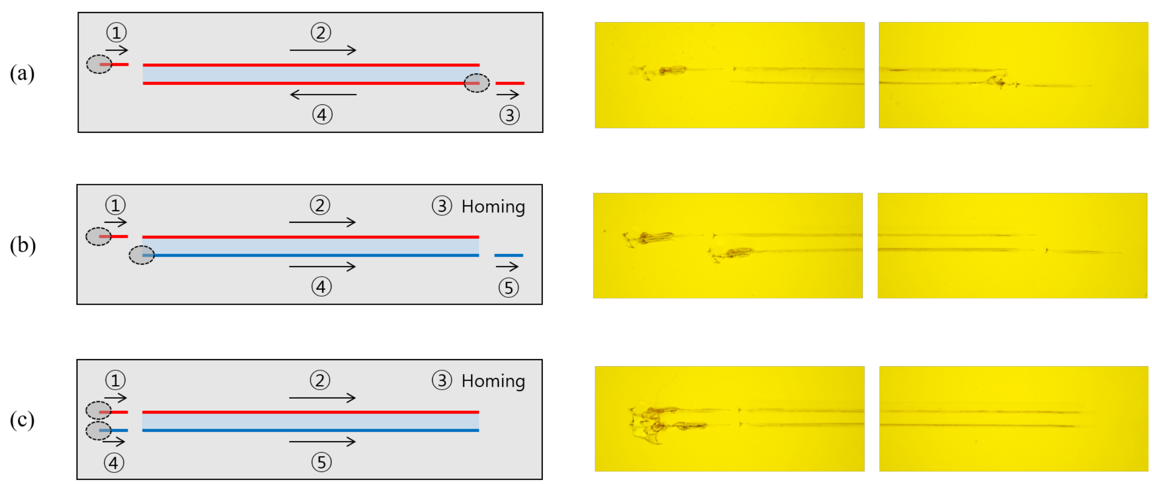

Figure 15: Cutting results for different cutting orders

Figure 15 shows different cutting group assignments and the cutting results for the flow channel. Damaged regions on the cutting result by the sudden changes in the razor direction are highlighted in the gray circles. Between each cutting group, the homing of the razor blade happens to calibrate the blade length which also results in the rotation on the razor. Additional short lines are added to allow the razor to rotate to the right angle before cutting the channel parts. As shown in the figure, (c) has the optimum cutting result.

Figure 16: Cutting group assignment for flow layer

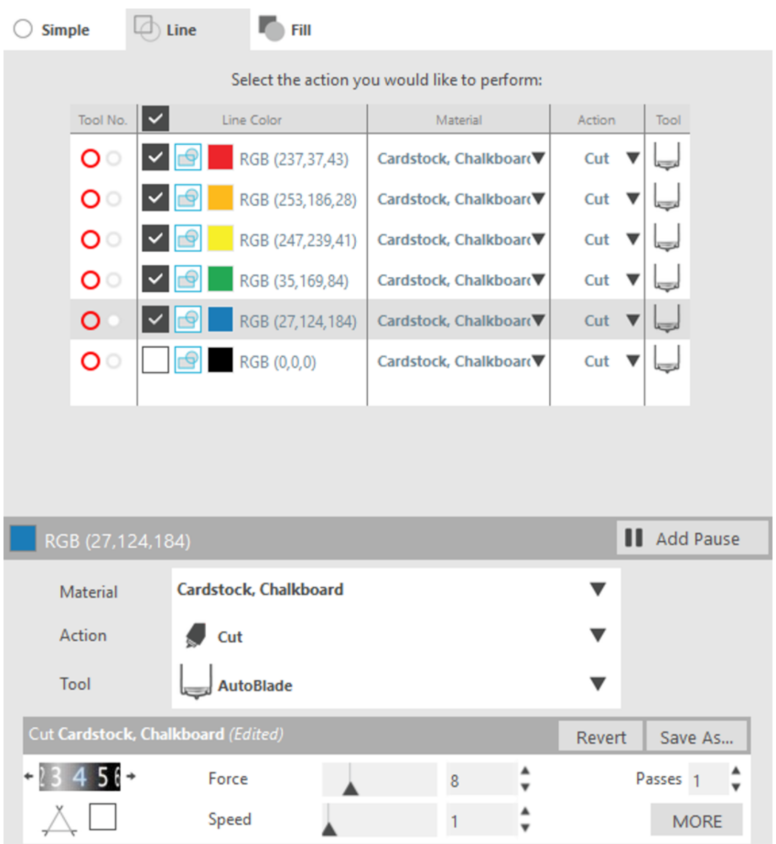

Figure 17: Silhouette Studio Design setting for flow layer

For the entire flow layer design, the cutting segments are assigned in five groups as Figure 16 and the Silhouette Studio Design is set as Figure 17 to specify the cutting order. Using this method, we were able to cut the flow layer with a standard deviation of less than 2 μm in the channel width.

Once the cut is complete, the channel negative and the circular part for the air inlet is removed using fine tweezers. The cut tape is placed over the top transparency and sealed ensuring the alignment of the inlet and the outlet holes with the transparency. Sufficiently long food wrap for the membrane layer is cut and gently swiped to remove dust. Then the liner on the tape is peeled off and the food wrap is attached on the tape. Pretension is not applied on the membrane in this thesis because of the limit on the pressure range we can apply from current setting.

The air layer is then cut by the craft cutter using the same setting as the flow layer. One should avoid cutting the air layer and the flow layer at the same time to minimize the contact time of the sticky side of the tape with the environment. The cut air layer is aligned with the flow layer ensuring that two channels share the same centerline and press seal on the membrane. The liner on the air layer is removed, and the acrylic sheet adheres to the tape.

Two sets of capillary tubing (Cole Parmer PTFE #30 AWG Thin wall tubing natural) and a gasket cut out of four layers of adhesive sheets (Aleene's instant tacky double-sided adhesive sheets) are adhered on the flow inlet and the air inlet using an epoxy adhesive (Parts express 5 Minute Quik-cure Epoxy adhesive).

Figure 18: Fabricated microchip

The order of the fabrication can be adjusted as need keeping in mind that it is important to adhere the membrane to the flow channel before adhering it to the air channel. Because the control channel is wider than the flow channel, it becomes hard to seal the tape near the flow channel wall if the membrane is already attached on the control channel.

4 Taylor dispersion experiment

4.1 Imaging methods

Fluorescence microscopy has been widely used in numerous fields of modern science including microfluidics due to its superior sensitivity and the linear relationship between the concentration of a fluorophore and its fluorescence intensity [19, 20]. However, the use of this technique requires a special excitation source such as a mercury lamp, and a microscope with filter system. While the system has many advantages for measurements requiring high accuracy, a variety of issues have to be considered [20]. A significant issue for the present experiments is the photobleaching effect which is a permanent loss of the ability for a fluorescent chemical compound to fluoresce. This effect can add significant error in the calibration between the intensity signal and the concentration field.

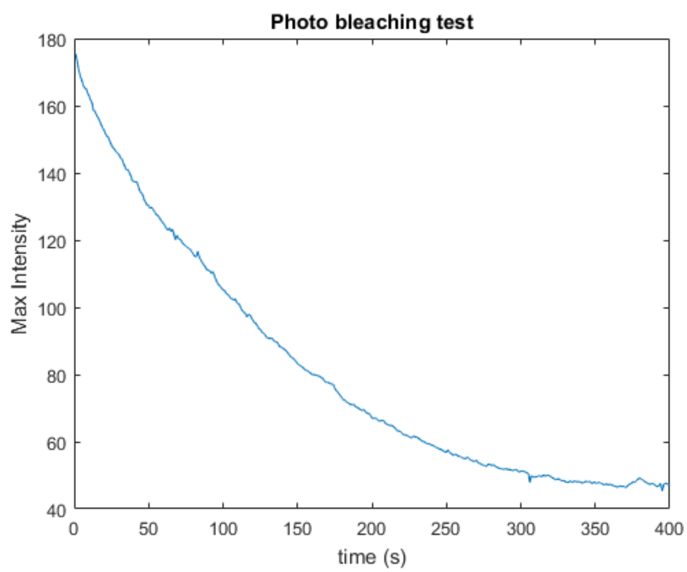

Figure 19: Photobleaching test result

Considering the disadvantages of using fluorescence microscopy such as photobleaching effect and uneven illumination, bright field imaging on a flat light panel has been chosen for this thesis. Since a white light emitted from a light panel is not specifically filter to excite the fluorescein molecules, the photobleaching effect becomes negligibly small on a light panel compared to fluorescence microscopy.

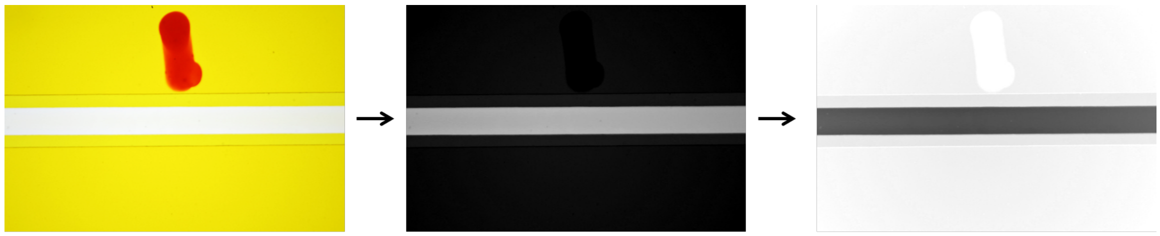

(a) (b) (c)

Figure 20: Image processing for bright filed imaging (a) Raw image, (b) Decomposed B channel, (c) Inversed result from (b)

To acquire the best contrast between the channel region and the yellow region where the double sided tape serves as channel boundaries, RGB channels are decomposed and compared. Among the three channels, the Blue (B) channel shows the best ability to distinguish the channel region.

In fluorescence microscopy, higher intensity represents a higher concentration of dye molecules along the light path. In the contrary, in bright field imaging, a larger number of dye molecules block the light coming through the channel which yields lower intensity measured from a camera. Hence, the B channel intensity values are inversed by subtracting from the maximum possible intensity value 255.

Fluorescein has been chosen because of its known molecular diffusivity κ, however, this imaging method can also be applicable with other sorts of dye such as food coloring for research that does not require a well-documented molecular diffusivity. The RGB channel separation result and the linearity validation are included in Appendix A.1. Solute intensity processed as above was calibrated to verify the linear relationship between the intensity and the product of the thickness of the channel and the concentration of the dye solution in the channel.

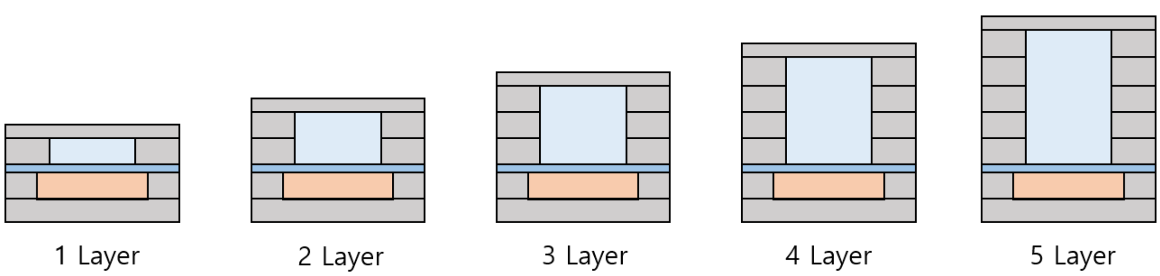

Figure 21: Multilayer microchip for intensity calibration

Channels of different thickness fabricated by changing the number of the double-sided tape layer shown in Figure 21 are filled with dye solutions with various concentration to obtain the data shown in Figure 22a.

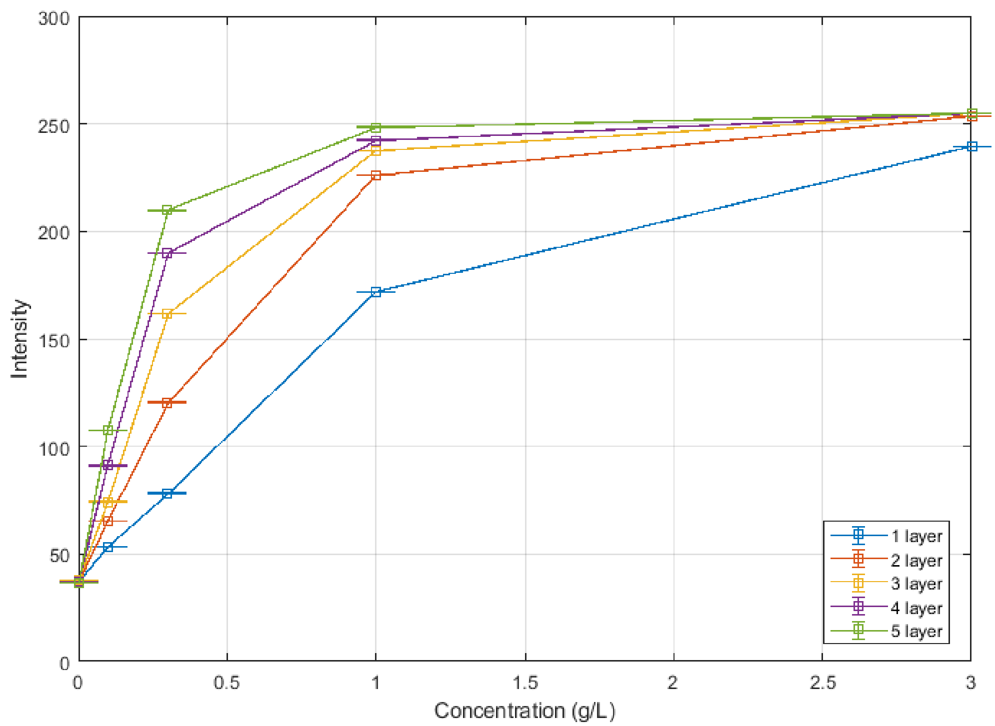

(a) Intensity calibration for different channel thickness

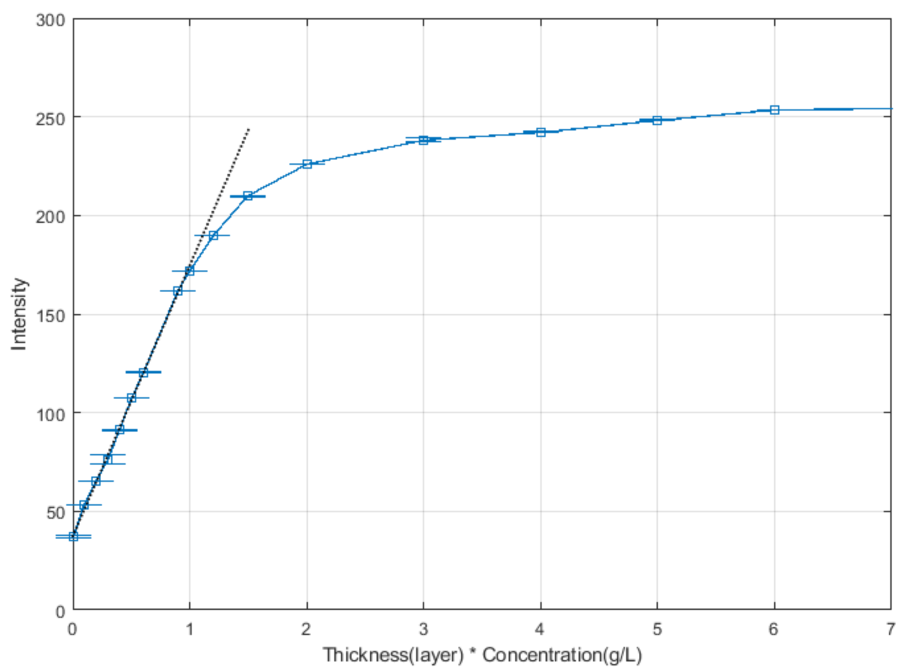

(b) Intensity calibration result in one master graph

Figure 22: Intensity calibration result

A robust linear regime was found below an intensity value of 160, after which the relationship becomes nonlinear. In this linear regime, we can translate the intensity signal into a measure of the concentration field. A best fit curve is used to extract the conversion within the linear regime and expressed by

$$\text{Intensity} = 138.17 \times (\text{Thickness [layer]}) \times (\text{Concentration [g/L]}) + 36.98$$

The number of the tape layer is used as a unit, which corresponds to the 101.6 μm in channel height. By filled with a known uniform concentration of fluorescein dye solution, we can use this relationship to measure the profile of the channel in the same setup.

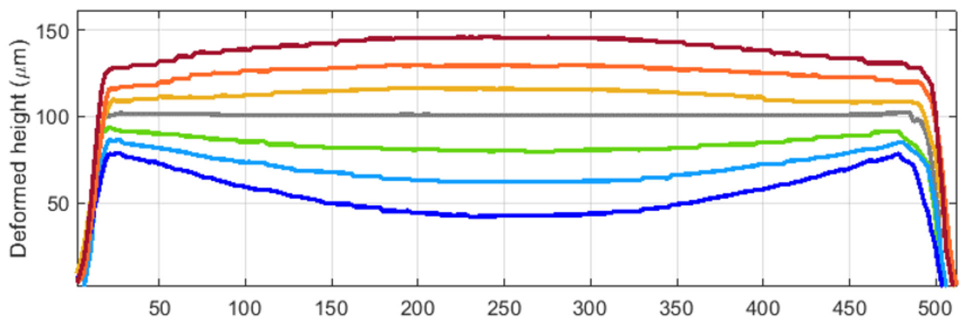

Figure 23: Deformed channel geometry measurement result.

Figure 23 is the measured channel geometry for 1:4.71 aspect ratio chip with different air pressure applied in the air channel. We observed deformation on the side walls as well as the membrane itself because of the elastic properties of the double-sided tape used as a channel boundary.

4.2 Experimental method

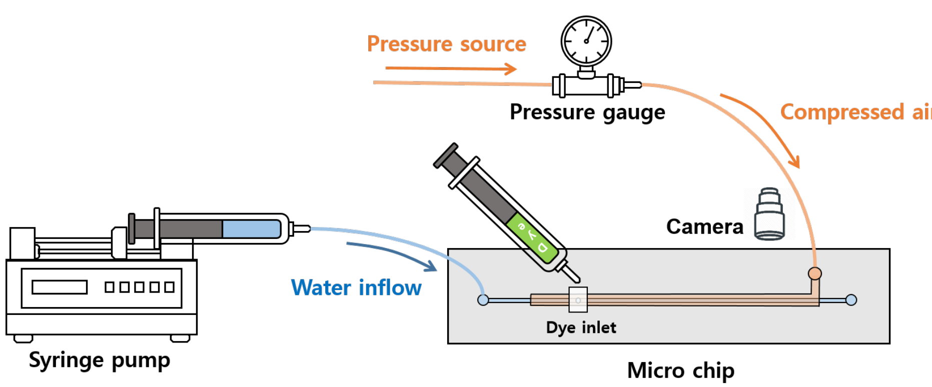

Figure 24: Schematic of the experimental setup

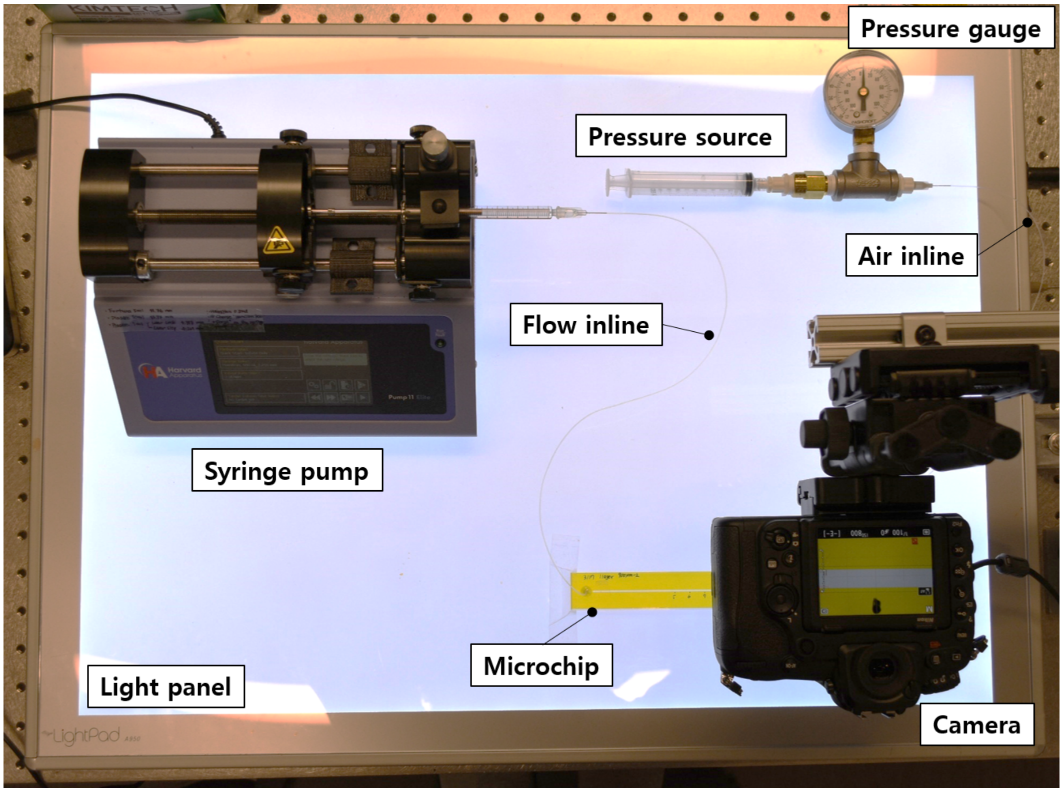

Figure 25: Experimental setup

The microchip is connected to a glass syringe installed on a syringe pump (Harvard apparatus Standard Infuse-Withdraw Pump 11 Elite) through a capillary tubing (Cole Parmer PTFE #30 AWG Thin wall tubing natural) and 27 Gauge blunt-tip needle. The air channel tubing is connected to the pressure source with the same tubing and the needle. The tubing has inner diameter of 0.30 mm and the needle has outer diameter of 0.41 mm ensuring a tight fit to prevent air and water leakage. The system is placed on 17 x 24 inch light panel (Artograph LightPad A950) to illuminate the microchip with even lighting. To capture the intensity changes in the channel, a camera (Nikon D 500) is placed vertically over the chip mounted on a focusing rail (Oben MFR4-5 Macro Focusing Rail) for precise camera alignment. The center of the frame is fixed at 15 cm downstream from the dye hole to ensure that the solute patch reaches the long-time asymptotic regime. For the flow velocity of 1 mm/s, the system is in the asymptotic regime after around 5 cm downstream calculated from Equation 8. A macro lens (Mitakon Zhongyi 20mm f/2 4.5x Super Macro Lens) is mounted on the camera to image the channel. The resolution of the images taken in this setup is 1.04 μm per pixel

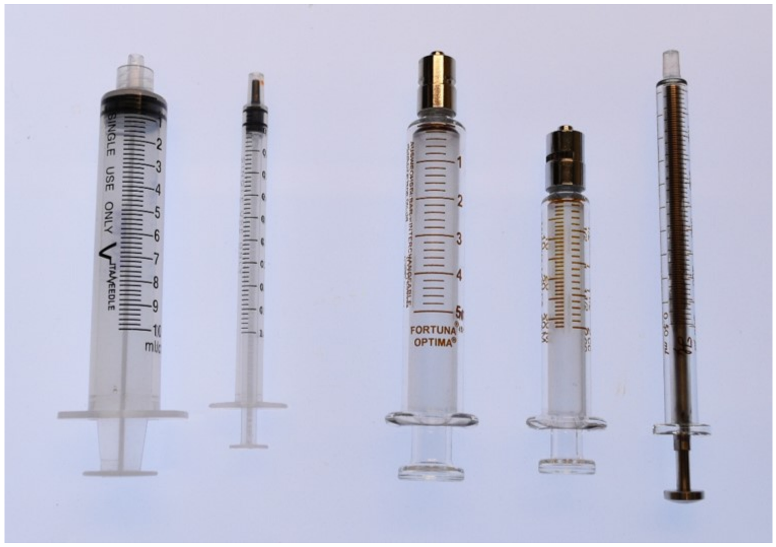

Figure 26: Different types of syringes (10 ml plastic, 1 ml plastic, 5 ml glass, 3 ml glass, and 0.5 ml glass syringe)

Typical plastic syringes have a rubber seal on the head of the plunger for sealing. When the syringe pump is operated with this type of syringe, the friction produced between the barrel and the plunger obstructs the immediate movement of the fluid in the syringe when the syringe pump begins to run. Thus, the use of a glass syringe is favorable over a plastic syringe.

The existence of a small gap between the plunger and the pusher block on the syringe pump allows the syringes to generate unwanted flow by freely moving in this gap when the pump is not running. This problem can be resolved by using a syringe with a small inner diameter which produces a smaller flow rate for the same displacement of the plunger. Since the stepper motor operating the syringe pump moves with a discrete step size, using a smaller diameter syringe also helps produce smoother fluid movement during the experiment.

While a syringe with a smaller diameter is beneficial to control undesired fluid movement, a syringe with enough volume is necessary to maintain the flow throught the entire dispersion experiment. Considering the trade-offs described above, a Hamilton 750 LT SYR syringe with a volume of 0.5 ml and an inner diameter of 3.256 mm was selected.

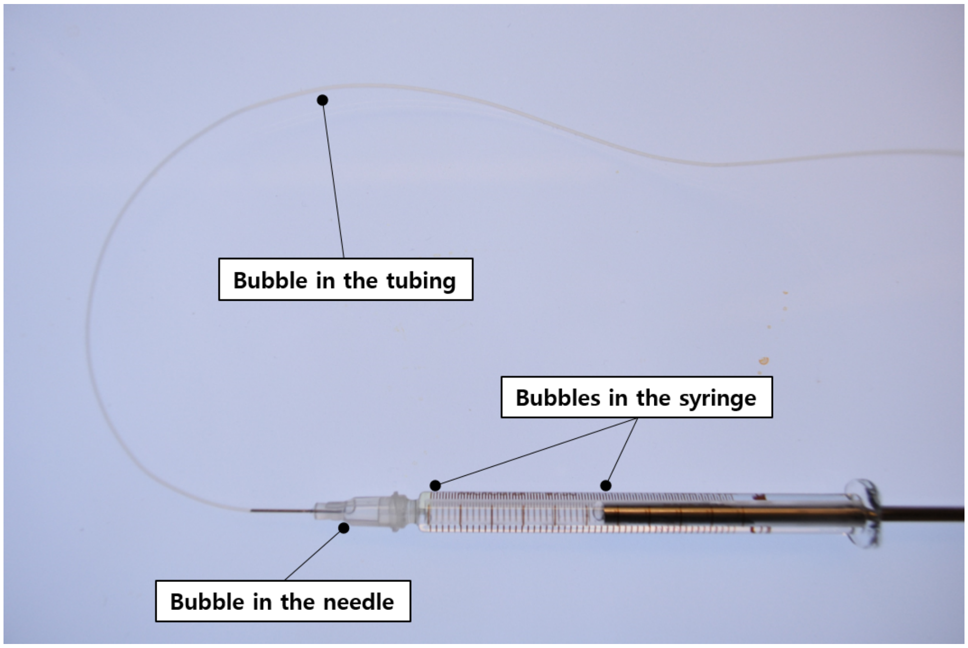

Figure 27: Bubbles in the system

In addition, any small bubbles along the fluid path should be avoided for precise control of the flow starting time and to prevent poorly controlled flow in the channel. Bubbles can be compressed during the first stage and delay the flow. More importantly, they can be apart from the wall where they were initially attached and form an air patch in the flow channel. This includes bubbles in the syringe, needle, tubing, and the flow channel. To avoid any bubbles to be formed, a syringe filled with isopropanol (IPA) is first connected to the system to flush any existing bubbles along the flow path. Once the bubbles are cleared, the IPA syringe is removed from the needle, and a water-filled syringe is connected ensuring no bubbles formation in the needle to flush out the IPA in the channel. We used at least 2 ml of water to wash out IPA in the channel. While IPA is a good option to remove bubbles because of its lower surface tension, this can also smear in between the polyimide tape and membrane or the PET top and eventually disassemble the fluid channel by weakening the attachment. Thus, the contact time between the channel and IPA should be minimized, and excessive pressure by a fast flow should be avoided at the same time.

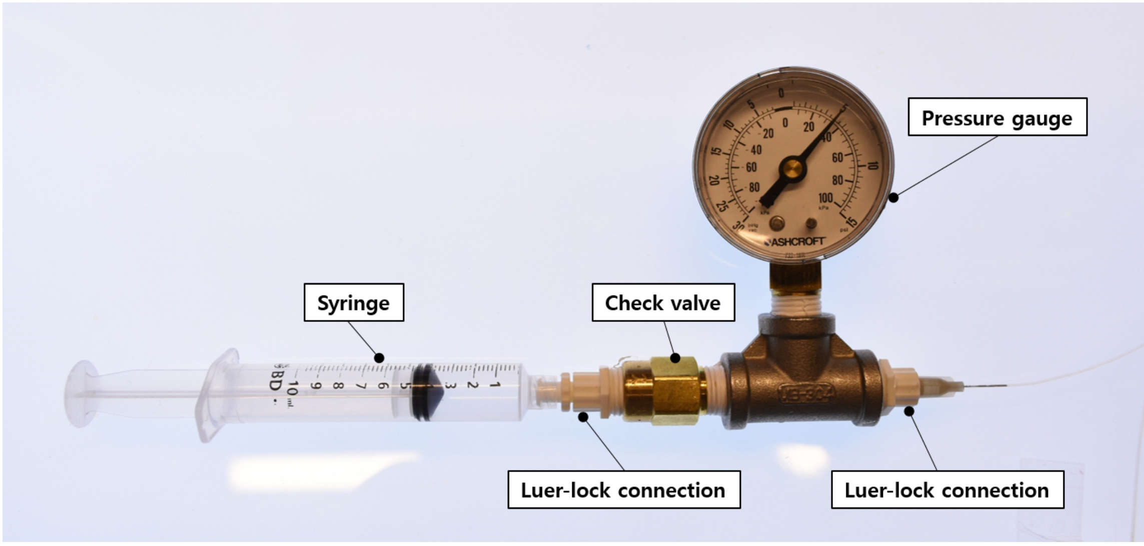

Figure 28: Pressure applying system

A syringe and a check valve connected through luer-lock connections are used to apply and hold a known static pressure in the air channel. The applied pressure is measured with a pressure gauge placed after the check valve, which is then connected to the air channel tubing by luer-lock connection again. One advantage of this system over a system with an air compressor and a pressure regulator is that air leakage in the system can be detected easily. With a pressure regulator, it is easier to keep a constant pressure when there is air leakage or fluid flow. However, we want the air channel to be a closed system during the experiment and want to notice if there is air penetration from the air channel to the flow channel through the membrane, which often occurs under high pressure.

Figure 29: Check valves

To apply positive pressure in the air channel, the check valve which allows the flow towards the right side is used, and the check valve of the opposite direction is used for applying negative pressure.

Once the syringe and the flow channel filled with water with no presence of any bubbles is prepared, the desired pressure is applied by adjusting the syringe connected to the air channel. Excessive water coming out from the outlet of the flow channel is swiped out to avoid a flow by hydrostatic pressure and the Laplace pressure from the bubble's height and the curvature. This step might seem to have a minor effect on the system; however, a small flow rate produced by any sources can generate a considerable fluid velocity because of the small dimensions of the channel.

After waiting for a minute to stabilize the system, the tape on the dye hole is removed, and a tiny droplet of fluorescein (HiMedia Laboratories Fluorescein sodium salt) solution with a known molecular diffusivity $\kappa = 5.7 \times 10^{-6} cm^2/s$ [11] is placed on the hole. A solution of 2g/L fluorescein is used in this thesis, however, the concentration has to be decided based on the dispersivity, camera settings, and the lighting as to not exceeding the linear limit of the concentration versus intensity at the measurement location and also to produce enough intensity to maximize the signal to noise ratio in the intensity signal. The hole is tape sealed again ensuring no bubble is formed near the hole. The initial dye patch in the flow channel should be no longer than 2 mm. By observing the movement of the dye patch once it is introduced, one can check if there is any undesired flow in the flow channel.

Figure 30: Syringe pump setting

On the syringe pump, 'Method Select' option is set to infusion and the correct syringe type is selected on the 'Syringe Select' option. The 'Infuse Rate' has to be calculated by multiplying the measured channel cross-sectional area of the flow channel and the desired flow velocity. In this thesis, a fixed flow velocity of 1 mm/s has been used. Considering that there exists a small gap between the plunger and the pusher block on the syringe pump, as well as some backlash in the pump drive itself, the last operation before starting the experiment should always be in the forward (infusion) direction.

Figure 31: Remote shutter release setup

A Nikon MC-36A Multi-function remote shutter release is used to control the delay before the imaging system collects the data, the interval between each data acquisition, and the number of images to be taken. ‘Long’ option on the shutter release which controls the shutter speed is set to zero which means the parameter will be controlled on the camera. The delay is set between 2 min to 4 min to minimize unwanted data to be collected. This value and the number of images should be determined experimentally based on trial and error to collect all the necessary data starting from the plateau, rising, falling, and the final plateau of the dye intensity.

On the camera, shutter speed is set to be 1/100 s with ISO 800, the ‘Image quality’ and ‘Image size’ are set as ‘JPEG Fine’ and ‘Large’. The macro lens is adjusted to have a fully opened aperture position of F2 with x4.0 magnification. Once the syringe pump, the shutter release, and the camera are set up, the syringe pump and the shutter release are started simultaneously.

4.3 Data analysis

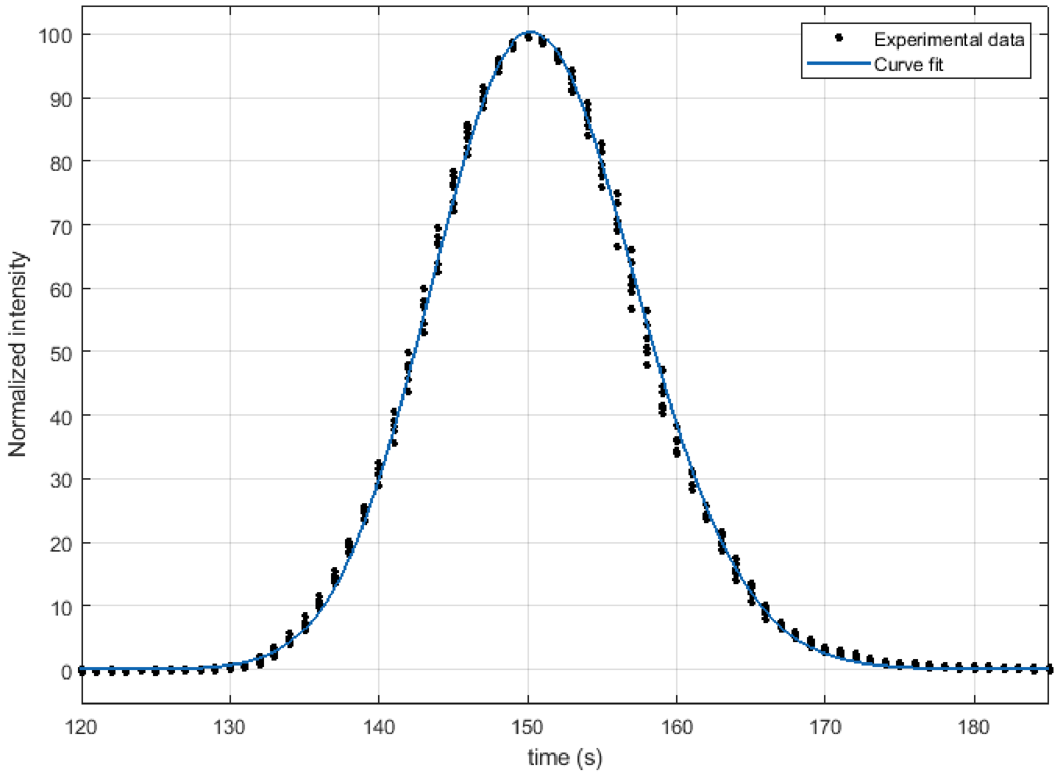

Figure 32: Curve fitting result for 1:7.41 chip with δ=-0.36

The intensity is recorded versus time at a fixed position of 15 cm downstream from the dye inlet. For each collected photos, the intensity is averaged over the area which is fit to the width of the channel and 100 pixels in the channel direction. The intensity profiles over time gathered from 7 independent trials are overlaid.

The collected intensity profiles are curve fit to the Gaussian distribution in long-time regime

$$c(t) = \frac{1}{\sqrt{4\pi K t}} \exp\left(\frac{(x_0 - Ut)^2}{4Kt}\right) \tag{19}$$

using a 'Curve Fitting Toolbox' in Matlab. The measurement position x_0 and the average velocity U are specified and only the dispersivity K is fit to obtain a best fit curve.

The dispersion factor f can thus ultimately calculated as

$$f = \frac{210}{Pe^2}\left(\frac{K}{\kappa} - 1\right) = 210\left(\frac{\kappa}{Ud}\right)^2\left(\frac{K}{\kappa} - 1\right) \tag{20}$$

4.4 Results

In this thesis, two microchips with different aspect ratios were studied. The measured widths of the flow channels are 488.6 μm and 750.5 μm, and the corresponding aspect ratios are 1:4.81 and 1:7.41, respectively. Theoretical values of dispersion factor f are numerically calculated by solving Equation 6 using the finite element package in Matlab. This computation was set up by our collaborators Alan Luner and Jeremy Marzuola at the University of North Carolina at Chapel Hill, Department of Mathematics. Theoretical values of dispersion factors are drawn in a solid black line, and experimental data are depicted with error bars drawn based on standard multivariable error analysis.

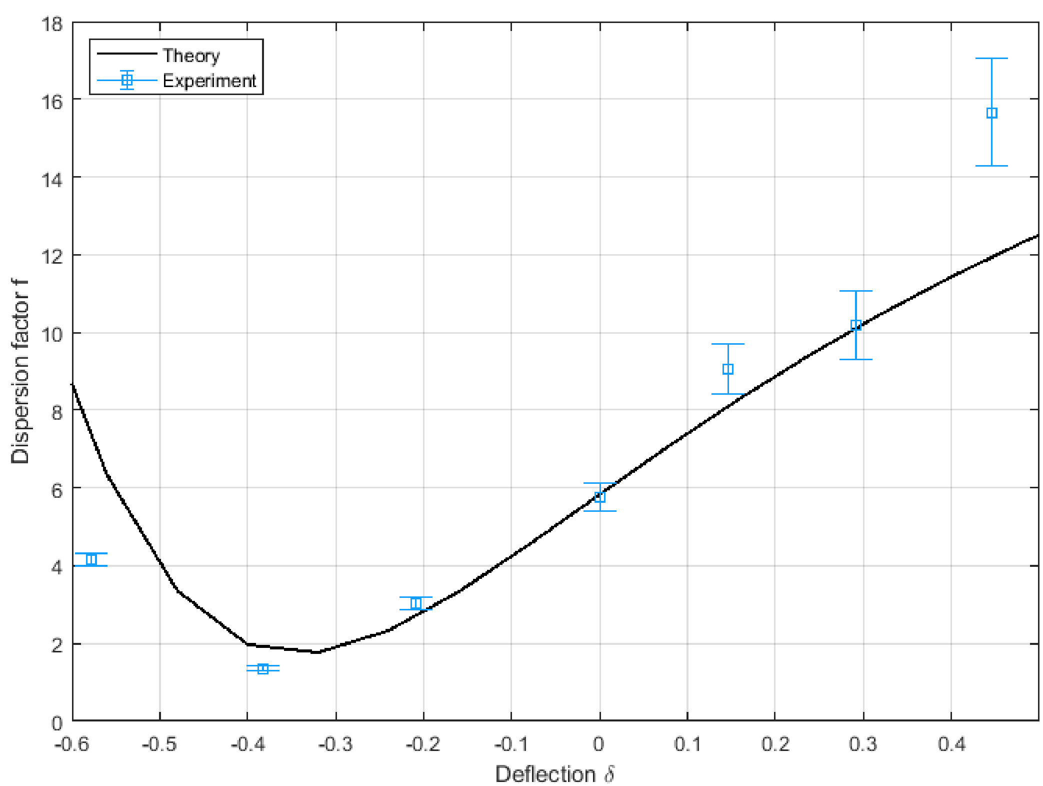

Figure 33: Dispersion factor versus Deflection in 1 : 4.81 chip

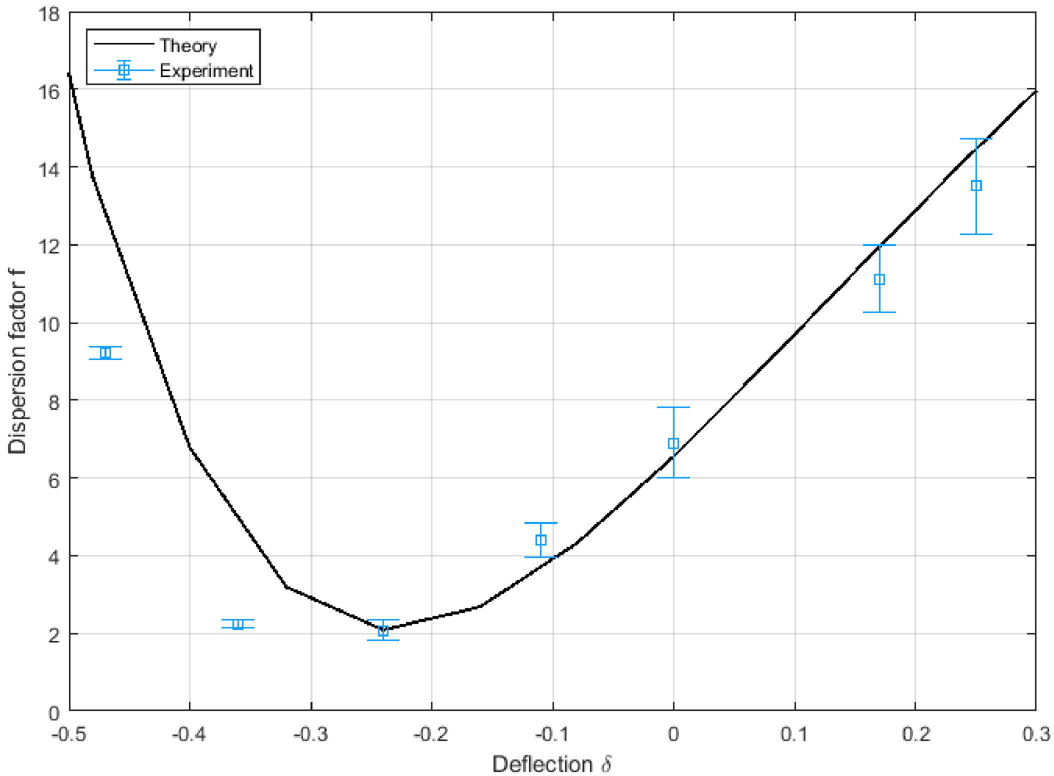

Figure 34: Dispersion factor versus Deflection in 1 : 7.41 chip

Figure 33 and Figure 34 show that the experiments on a single chip yield very close values of the dispersion factor f as compared to the theoretical values. This gives us confidence in predictable control of the dispersion factor in such a system.

In both cases, a minimum of f values are observed in experiments which were also predicted in theoretical calculation. This suggests that we are able to minimize the dispersion effect by deforming a sidewall in a fixed aspect ratio channel operated with the same flow velocity. The wider channel shows a larger dispersion factor at the minimum, and the value increases steeper than the narrower channel.

Specifically, the minimum points on the dispersion factor f in theory are

$$\begin{aligned} &\text{For 1:4.81 chip,} \quad f_{the} = 1.97 \quad at \quad \delta = -0.32 \\ &\text{For 1:7.41 chip,} \quad f_{the} = 2.09 \quad at \quad \delta = -0.24 \end{aligned} \tag{21}$$

The smallest dispersion factors measured from the experiments are

$$\begin{aligned} &\text{For 1:4.81 chip,} \quad f_{exp} = 1.36 \pm 0.06 \quad at \quad \delta = -0.38 \\ &\text{For 1:7.41 chip,} \quad f_{exp} = 2.08 \pm 0.26 \quad at \quad \delta = -0.24 \end{aligned} \tag{22}$$

Since we used a fixed flow velocity of 1 mm/s through all experiments, the trend in the dispersion factor can also be translated to the dispersivity in each channel shape which is correlated to the length of the solute band in the channel direction.

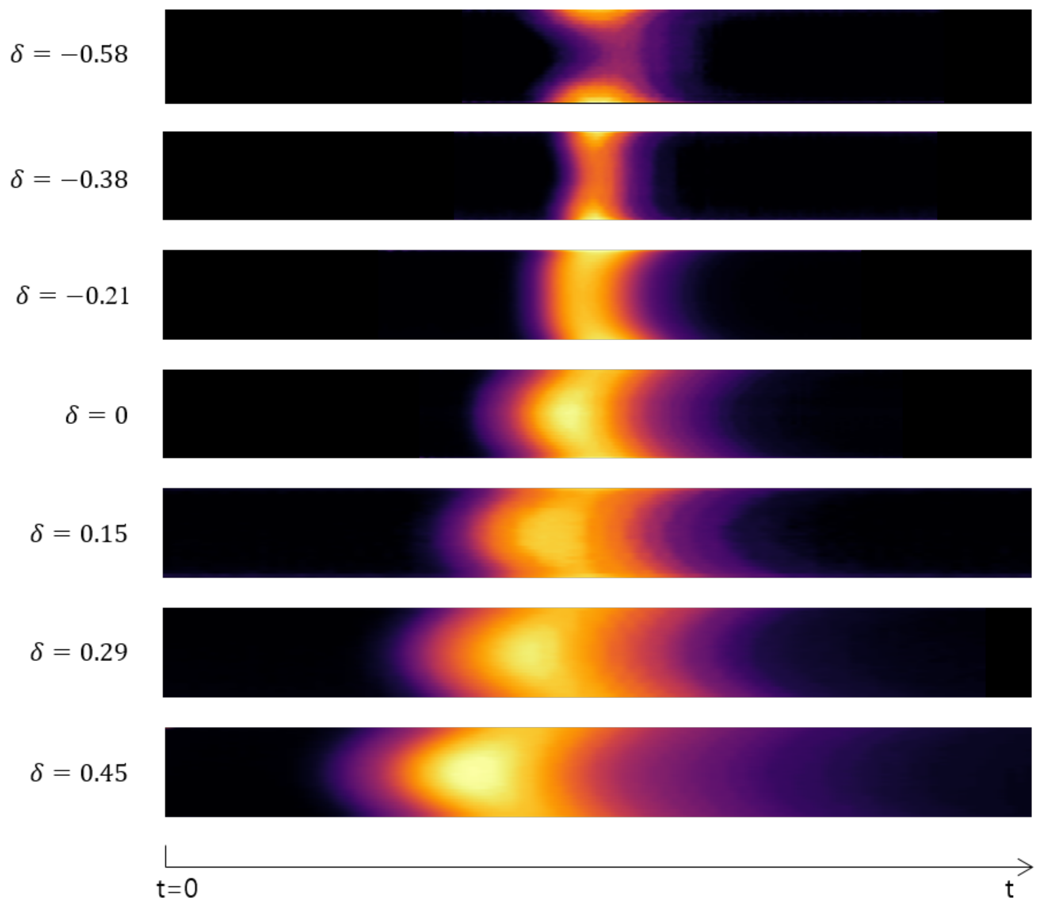

Figure 35: Intensity profile change over time in 1:4.81 chip

Figure 35 shows the intensity profile change over time for seven different δ values corresponding to the data from Figure 33. Note that the figure is a reconstruction of intensity profiles measured at a fixed spatial location.

5 Conclusion

5.1 Limitations

5.1.1 Skewed intensity profile

In long-time asymptotic regime, the intensity profile of the dye patch along the channel direction should converge towards a simple Gaussian distribution. However, we observed notably skewed intensity profiles for cases with positive deflection parameter δ. The profile becomes more skewed with larger deflection parameter δ and wider channel geometry. While significant skewness is not present for the data used in this thesis, preliminary data obtained from a wider channel showed significant skewness in the intensity profile and a notably worse fit to our expected Gaussian expression. Recall that in a rectangular channel, the dispersivity approaches 95% of its asymptotic value after the time below [6].

$$t \sim \frac{1}{20}\frac{W^2}{\kappa}$$

This value was used as a criterion to determine how far the solute patch should travel before measuring the intensity profile. However, this has been verified numerically only in rectangular channels which is likely different for the deformed channel shape considered in our work.

If the time required to reach its asymptotic regime is longer in the deformed channel shape than the rectangular channel, it is possible that the system is still in the transient time regime at our current measurement point.

5.1.2 Deformed channel geometry different from theory

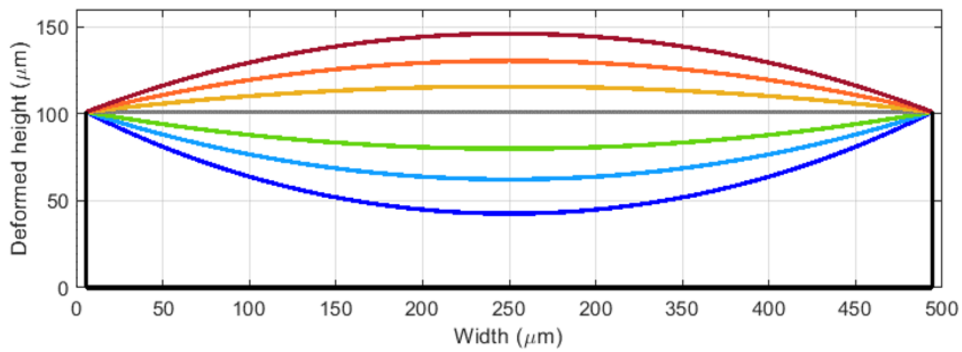

Figure 36: Ideal channel geometry with deformation for 1:4.81 chip

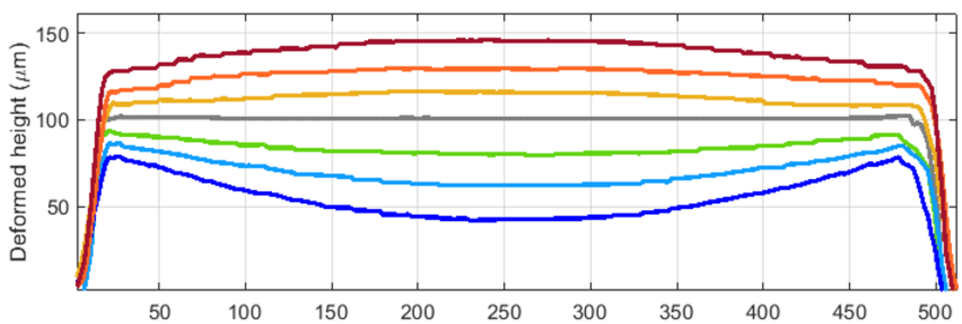

Figure 37: Measured channel geometry with deformation for 1:4.81 chip

The theoretical values are calculated based on an idealized deformed channel shape that is defined by only two parameters: the aspect ration and the deflection parameter. However, the channel geometry measured from the experiment shows that the side walls also undergo some deformation due to the elasticity of the double-sided tape. The discrepancy between the idealized shape and the measured shape is a direct result of this stretching and compression of the channel sidewalls.

In addition, the deformed membrane curve used in the numerical calculation of dispersion factor f for a given geometry was determined based on a parabolic shape which is not necessarily true for the real channel geometry. Though we expect the effect of the parabolic assumption on the result to be small, this assumption may also contribute to the small discrepancies observed.

5.2 Future work

To reduce the skewness observed in the channel with larger deflection, the measurement site should be placed more downstream which requires even longer channel than the current design. We utilized the craft cutter with its maximum possible cutting length; therefore, other craft cutters with longer working distance or other methods to fabricate a longer channel has to be implemented to resolve this problem. Also, a proper justification of the necessary time required to reach the asymptotic regime in a deformed channel shape is required to further evaluate and refine the experimental design.

A difference between the deformed channel geometry used in the calculation and the measured geometry has also been noted. The most significant difference results from the sidewall deflection due to the high pressure difference applied on the channel's elastic sidewalls. On the experimental side, we can try different membrane materials which require less pressure to reach the same deflection. Also, the numerical computation method can be readily adjusted to incorporate the measured geometry into the calculation.

For future experiments, a wider variety of aspect ratios will be explored. More exotic channel geometries to optimize the dispersion factor could also be studied. Changing the data acquisition method from capturing a series of data over time at a fixed spatial location to taking a photos of the entire channel could simplify the curve fitting process and also to acquire more quantitative information about the distribution such as the skewness.

5.3 Summary

This thesis has established a method to control a dispersion factor within a single microchannel by deforming one of the channel walls. The fabrication technique uses a craft cutter which allows us to achieve this goal without relying on the expensive equipment and facilities required by other common microfabrication techniques.

Through numerical calculation and experiment, we were able uncover an a sensitive relationshop between the dispersion factor f and wall deflection deflection parameter δ. The minimum value of f was found when one of the channel wall was deformed inward by $\delta \sim -0.3$ in both $1:4.81$ and $1:7.41$ aspect ratio channels.

References

[1] R. M. van Dam. *Solvent-resistant elastomeric microfluidic devices and applications*. PhD thesis, 2006.

[2] P. M. Fordyce, C. A. Diaz-Botia, J. L. DeRisi, and R. Gomez-Sjoberg. Systematic characterization of feature dimensions and closing pressures for microfluidic valves produced via photoresist reflow. *Lab on a Chip*, 2012.

[3] G. I. Taylor. Dispersion of soluble matter in solvent flowing slowly through a tube. *The Royal Society*, 1953.

[4] N. Bontoux, A. Pépin, Y. Chen, A. Ajdari, and H. A. Stone. Experimental characterization of hydrodynamic dispersion in shallow microchannels. *Lab on a Chip*, 2006.

[5] R. A. Wooding. Instability of a viscous liquid of variable density in a vertical hele-shaw cell. *Journal of Fluid Mechanics*, 1959.

[6] D. Dutta and D. T. Leighton Jr. Dispersion reduction in pressure-driven flow through microetched channels. *Analytical Chemistry*, 2001.

[7] D. Dutta, A. Ramachandran, and D. T. Leighton Jr. Effect of channel geometry on solute dispersion in pressure-driven microfluidic systems. *Microfluid Nanofluid*, 2006.

[8] J. Aubin, L. Prat, C. Xuereb, and C. Gourdon. Effect of microchannel aspect ratio on residence time distributions and the axial dispersion coefficient. *Chemical Engineering and Processing: Process Intensification*, 2008.

[9] M. Callewaert, W. De Malsche, H. Ottevaere, H. Thienpont, and G. Desmet. Assessment and numerical search for minimal taylor–aris dispersion in micro-machined channels of nearly rectangular cross-section. *Journal of Chromatography A*, 2014.

[10] P. C. Chatwin and P. J. Sullivan. The effect of aspect ratio on longitudinal diffusivity in rectangular channels. *Journal of Fluid Mechanics*, 1981.

[11] M. Aminian, F. Bernardi, R. Camassa, D. M. Harris, and R. M. Mclaughlin. How boundaries shape chemical delivery in microfluidics. *Science*, 2016.

[12] R. Aris. On the dispersion of a solute in a fluid flowing through a tube. *Proceedings of the Royal Society of London A*, 1955.

[13] W. N. Gilland and R. Sankarasubramanian. Exact analysis of unsteady convective diffusion. *Proceedings of the Royal Society of London A*, 1969.

[14] H. Liu and H. Gong. Templateless prototyping of polydimethylsiloxane microfluidic structures using a pulsed co_2 laser. *Journal of Micromechanics and Microengineering*, 2009.

[15] A. W. Taylor and D. M. Harris. Optimized commercial desktop cutter technique for rapid-prototyping of microfluidic devices and application to taylor dispersion. *Review of Scientific Instruments*, 2019.

[16] P. Yuen and V. N. Goral. Low-cost rapid prototyping of flexible microfluidic devices using a desktop digital craft cutter. *Lab on a Chip*, 2009.

[17] M. A. Unger, H. Chou, T. Thorsen, A. Scherer, and S. R. Quake. Monolithic microfabricated valves and pumps by multilayer soft lithography. *Science*, 2000.

[18] Cambridge University Engineering Department. *Materials Data Book*, 2003 edition edition.

[19] B. Kuswandi, Nuriman, J. Huskens, and W. Verboom. Optical sensing systems for microfluidic devices: A review. *Analytica Chimica Acta*, 2007.

[20] G. liebsch G. Neurauter A. Strangelmayer O. S. Wolfbeis I. Klimant, C. Huber. *Dual Lifetime Referencing (DLR) - a New Scheme for Converting Fluorescence Intensity into a Frequency-Domain or Time-Domain Information*. New Trends in Fluorescence Spectroscopy, Applications to Chemical and Life Sciences. Springer, 2001.

A Appendix

A.1 Food coloring RGB decomposition comparison

Figure 38: Food coloring options

RGB decomposition results are placed in the order of the dye solution arranged according to FigureFood from left to right. First column shows the raw image, and the seconde to the last column depict R, G, B Channel intensity profile averaged over the image width. Blue line represents the intensity profile when the channel is filled with pure water, green line represents the intensity with dye solution filled. Pink and Red lines the intensity across the channel when the pressurized air is applied in the air channel.

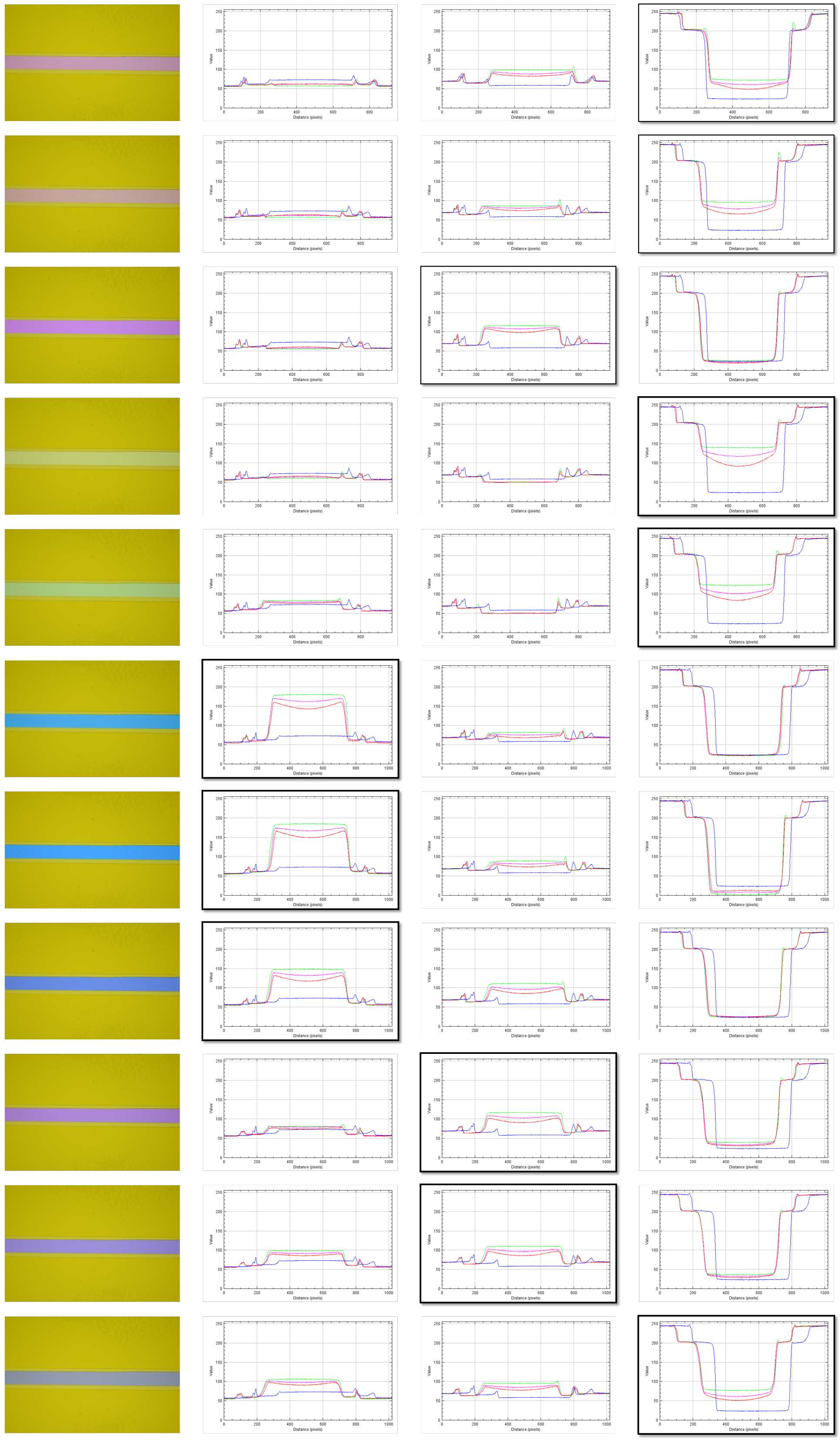

Figure 39: Food coloring RGB seperation

Intensity calibration is done for 'Blue Apple' color which shows the best contrast between the tape and the channel region.

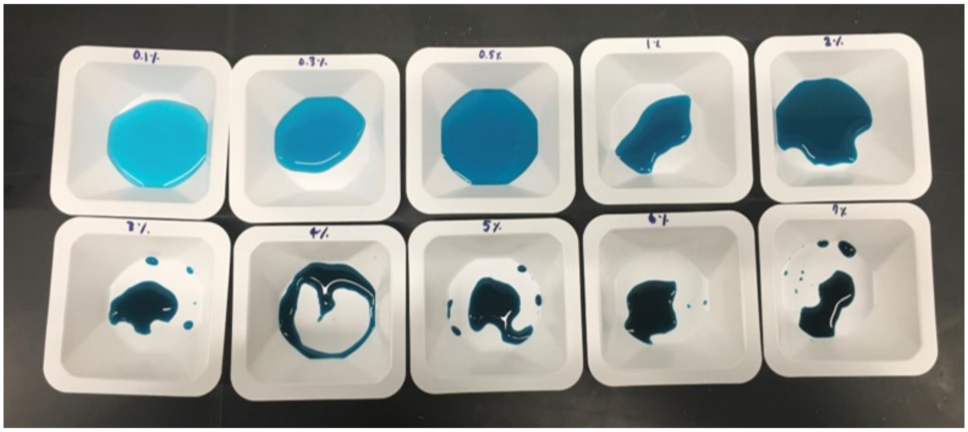

Figure 40: Intensity calibration setup for 'Blue apple' color

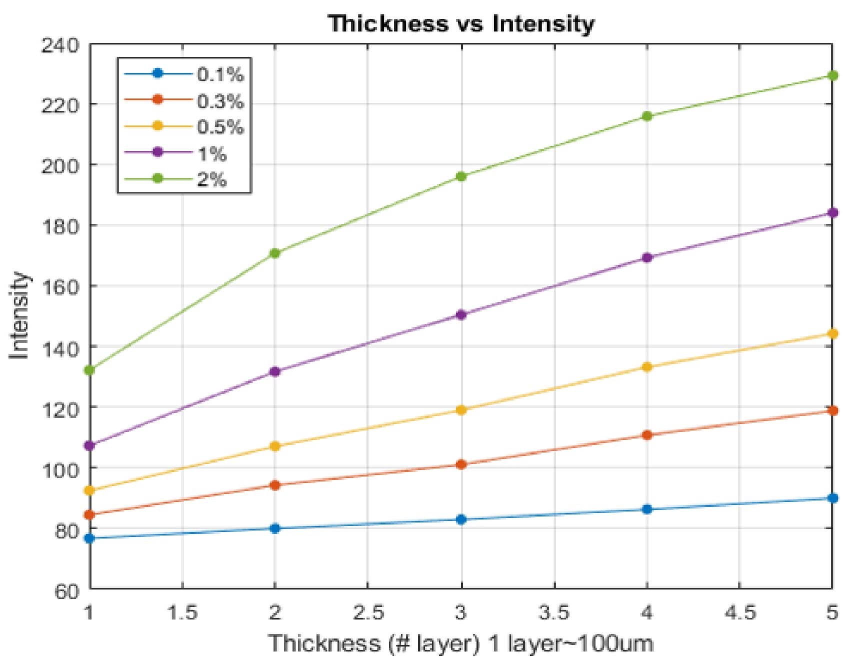

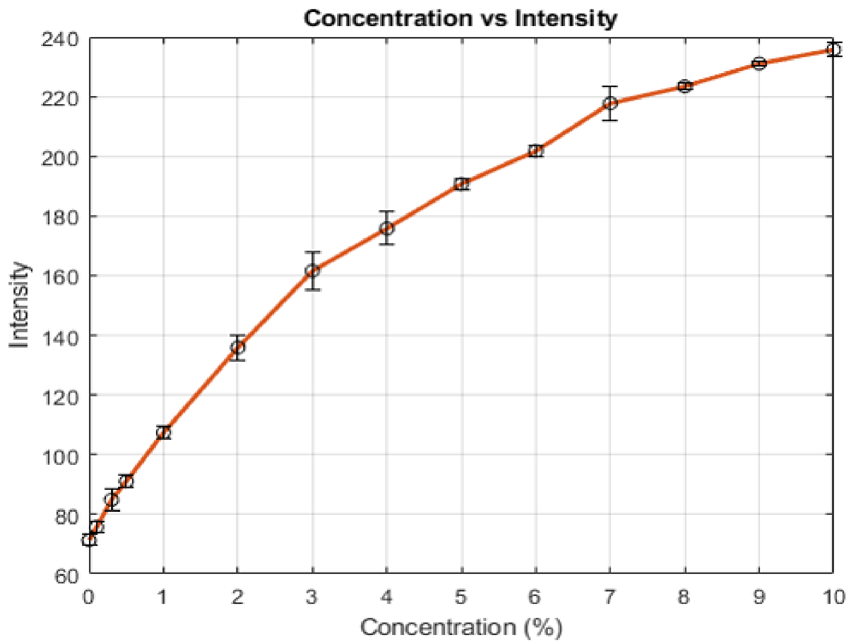

Figure 41: Intensity calibration result for 'Blue apple' color

A.2 Numerical solution for membrane deformation

```
[breaklines=true]

%%%%%%% Python code %%%%%%%

import scipy

from scipy.sparse import linalg

import matplotlib.pyplot as plt

import numpy as np

from mpl_toolkits.mplot3d import Axes3D

np.set_printoptions(precision=2)

from matplotlib import rcParams

rcParams.update({'figure.autolayout': True})


def rect_only_2nd(D,Tx,Ty,Nx,Ny,Lx,Ly,f0):

    nx = Nx - 2

    ny = Ny - 2
```

```
 hx = Lx/(Nx-1)
 hy = Ly/(Ny-1)

 x = np.linspace(0,Lx,Nx)
 y = np.linspace(0,Ly,Ny)
 X,Y = np.meshgrid(x,y)

########### Laplacian(u) coefficient matrix ###########
 a = Tx/hx**2
 b = Ty/hy**2

 e1_2nd = [-2*a - 2*b] * (nx*ny)
 e2_2nd = ([0] + [a]*(nx-1)) * ny

 f_2nd = [b] * (nx*ny)

 D_2nd = np.diag(e1_2nd,0) + np.diag(e2_2nd[1:],-1) + np.diag(e2_2nd[1:],1) + ...
 np.diag(f_2nd[nx:],nx)+np.diag(f_2nd[nx:],-nx)
 D_2nd = - D_2nd

 b_2nd = - np.ones(nx*ny)*f0

 #################### Solve #####################
 u0 = np.zeros([nx*ny])
 u,info = scipy.sparse.linalg.cg(D_2nd,b_2nd,u0)
 u = scipy.linalg.solve(D_2nd,b_2nd)

 u_matrix = u.reshape([ny,nx])
```

```
u_star = np.vstack([[np.zeros(nx)],u_matrix,[np.zeros(nx)]])
u_final = np.hstack([np.zeros([ny+2,1]), u_star, np.zeros([ny+2,1])])

return u_final, x,y,X,Y,nx,ny,Lx,Ly
#return D_2nd,b_2nd

def rect_only_bih(D,Tx,Ty,Nx,Ny,Lx,Ly,f0):
nx = Nx - 2
ny = Ny - 2
hx = Lx/(Nx-1)
hy = Ly/(Ny-1)

x = np.linspace(0,Lx,Nx)
y = np.linspace(0,Ly,Ny)
X,Y = np.meshgrid(x,y)

########### Biharmonic coefficient matrix #############
p = 6/hx**4 + 8/(hx**2*hy**2) + 6/hy**4
q = -4*(1/hx**2 + 1/hy**2)
r = 2/(hx**2*hy**2)

b1 = [p + (1/hx**4 + 1/hy**4)] + [p + 1/hy**2]*(nx -2) + [p + (1/hx**4 + 1/hy**4)]\
+ ([p + 1/hx**4] + [p]*(nx -2) + [p + 1/hx**4]) * (ny-2)\
+ [p + (1/hx**4 + 1/hy**4)] + [p + 1/hy**2]*(nx -2) + [p + (1/hx**4 + 1/hy**4)]

b2 = ([0] + [q/hx**2]*(nx-1)) * ny
b3 = ([0]*2 + [1/hx**4]*(nx-2)) *ny
```

```
c1 = [q/hy**2]*(nx*ny)
c2 = ([0] + [r]*(nx-1))*ny + [0]
c3 = ([0] + [r]*(nx-1))*ny

d = [1/hy**4]*(nx*ny - 2*nx)

D_4th = np.diag(b1,0) + np.diag(b2[1:],1) + np.diag(b2[1:],-1) ...
+ np.diag(b3[2:],2) + np.diag(b3[2:],-2) \
+ np.diag(c1[nx:],nx) + np.diag(c1[nx:],-nx) + np.diag(c2[nx:],nx-1)...
+ np.diag(c2[nx:],-(nx-1)) + np.diag(c3[nx+1:],nx+1) + np.diag(c3[nx+1:],-(nx+1))\
+ np.diag(d,2*nx) + np.diag(d,-2*nx)
D_4th = D * D_4th

b_4th = -np.ones(nx*ny)*f0

#################### Solve ######################
u0 = np.zeros([nx*ny])
u,info = scipy.sparse.linalg.cg(D_4th,b_4th,u0)

u_matrix = u.reshape([ny,nx])
u_star = np.vstack([[np.zeros(nx)],u_matrix,[np.zeros(nx)]])
u_final = np.hstack([np.zeros([ny+2,1]), u_star, np.zeros([ny+2,1])])

return u_final, x,y,X,Y,nx,ny,Lx,Ly

def rect_2nd_bih(D,Tx,Ty,Nx,Ny,Lx,Ly,f0):
nx = Nx - 2
ny = Ny - 2
```

```
hx = Lx/(Nx-1)
hy = Ly/(Ny-1)

x = np.linspace(0,Lx,Nx)
y = np.linspace(0,Ly,Ny)
X,Y = np.meshgrid(x,y)

########### Biharmonic coefficient matrix #############
p = 6/hx**4 + 8/(hx**2*hy**2) + 6/hy**4
q = -4*(1/hx**2 + 1/hy**2)
r = 2/(hx**2*hy**2)

b1 = [p + (1/hx**4 + 1/hy**4)] + [p + 1/hy**2]*(nx -2) + [p + (1/hx**4 + 1/hy**4)]\
+ ([p + 1/hx**4] + [p]*(nx -2) + [p + 1/hx**4]) * (ny-2)\
+ [p + (1/hx**4 + 1/hy**4)] + [p + 1/hy**2]*(nx -2) + [p + (1/hx**4 + 1/hy**4)]
b2 = ([0] + [q/hx**2]*(nx-1)) * ny
b3 = ([0]*2 + [1/hx**4]*(nx-2)) *ny

c1 = [q/hy**2]*(nx*ny)
c2 = ([0] + [r]*(nx-1))*ny + [0]
c3 = ([0] + [r]*(nx-1))*ny

d = [1/hy**4]*(nx*ny - 2*nx)

D_4th = np.diag(b1,0) + np.diag(b2[1:],1) + np.diag(b2[1:],-1) ...
+ np.diag(b3[2:],2) + np.diag(b3[2:],-2) \
+ np.diag(c1[nx:],nx) + np.diag(c1[nx:],-nx) + np.diag(c2[nx:],nx-1) ...
+ np.diag(c2[nx:],-(nx-1)) + np.diag(c3[nx+1:],nx+1) + np.diag(c3[nx+1:],-(nx+1))\
```

```
+ np.diag(d,2*nx) + np.diag(d,-2*nx)
D_4th = D * D_4th

b_4th = -np.ones(nx*ny)*f0

########### Laplacian(u) coefficient matrix ###########
a = Tx/hx**2
b = Ty/hy**2

e1_2nd = [-2*a - 2*b] * (nx*ny)
e2_2nd = ([0] + [a]*(nx-1)) * ny

f_2nd = [b] * (nx*ny)

D_2nd = np.diag(e1_2nd,0) + np.diag(e2_2nd[1:],-1) + np.diag(e2_2nd[1:],1) ...
+ np.diag(f_2nd[nx:],nx)+np.diag(f_2nd[nx:],-nx)
D_2nd = D_2nd

b_2nd = -np.ones(nx*ny)*f0

########### Sum of two #########
D_both = - D_2nd + D_4th
b_both = b_2nd

######## Solve ########
u0 = np.zeros([nx*ny])
u,info = scipy.sparse.linalg.cg(D_both,b_both,u0)
```

```
    u_matrix = u.reshape([ny,nx])
    u_star = np.vstack([[np.zeros(nx)],u_matrix,[np.zeros(nx)]])
    u_final = np.hstack([np.zeros([ny+2,1]), u_star, np.zeros([ny+2,1])])

    return u_final, x,y,X,Y,nx,ny,Lx,Ly
#    return D,b

def anal_sol(D,x,y,f0):
    sum = 0
    for n in range(1, 15):
        if(n % 2 != 0):
            sum = sum + 1/n**3*(1 - np.cosh(n*np.pi*x/Ly)/np.cosh(n*np.pi*Lx/(2*Ly))) ...
            *np.sin(n*np.pi*y/Ly)

    u_anal = (4/np.pi**3)*f0*Ly**2*sum
    return u_anal

def anal_plot(D,Nx,Ny,Lx,Ly,f0):
    x = np.linspace(0,Lx,Nx) - Lx/2
    y = np.linspace(0,Ly,Ny)
    X,Y = np.meshgrid(x,y)



    u_anal = np.zeros((Nx,Ny))
    for i in range(Nx):
        for j in range(Ny):
            u_anal[i,j] = anal_sol(D,x[i],y[j],f0)
    u_anal = u_anal.T
```

```
    return u_anal,x,y,X,Y,nx,ny,Lx,Ly

D = 0.001
Tx = 1
Ty = 1

Nx = 51
Ny = 11

Lx = 8
Ly = 1
f0 = 1

#u_2nd, x,y,X,Y,nx,ny,Lx,Ly = rect_only_2nd(D,Tx,Ty,Nx,Ny,Lx,Ly,f0)
#u_4th, x,y,X,Y,nx,ny,Lx,Ly = rect_only_bih(D,Tx,Ty,Nx,Ny,Lx,Ly,f0)
u_both, x,y,X,Y,nx,ny,Lx,Ly = rect_2nd_bih(D,Tx,Ty,Nx,Ny,Lx,Ly,f0)
#u_anal, xa,ya,Xa,Ya,nx,ny,Lx,Ly = anal_plot(D,Nx,Ny,Lx,Ly,f0)

from matplotlib import gridspec

fig = plt.figure(figsize=(8,1.5), dpi=100)
gs = gridspec.GridSpec(1, 2, width_ratios=[Lx,Ly])
xmid = int((nx-1)/2)
ymid = int((ny-1)/2)

ax1 = plt.subplot(gs[0])
#ax1.plot(xa+Lx/2,u_anal[ymid,:])
ax1.plot(x,u_both[ymid,:],'black')
```

```
#ax1.plot(x,u_2nd[ymid,:],'tab:blue',linestyle='--')
#ax1.plot(x,u_4th[ymid,:],'tab:orange',linestyle='--')

#ax1.set_title('Cross sectional view @ y=0.5')
ax1.set_xlabel('x'), ax1.set_ylabel('Deflection')
ax1.set_xlim([0,Lx]), #ax1.set_ylim([-0.005,0.0002])

ax2 = plt.subplot(gs[1])
#ax2.plot(ya,u_anal[:,xmid],label='2nd Analytical')
ax2.plot(y,u_both[:,xmid],'black',label='2nd + 4th')
#ax2.plot(y,u_2nd[:,xmid],'tab:blue',linestyle='--',label='Only 2nd')
#ax2.plot(y,u_4th[:,xmid],'tab:orange',linestyle='--',label='Only 4th')

#ax2.set_title('Cross sectional view @ x=0.5')
ax2.set_xlabel('y'), #ax2.set_ylabel('Deflection')
ax2.set_xlim([0,Ly]), #ax2.set_ylim([-0.005,0.0002])
plt.tick_params(axis='y',labelleft=False)
#ax2.legend(loc='center left', bbox_to_anchor=(1.1, 0.5))

flag='D=%s '%str(D) + 'Tx=%s '%str(Tx) + 'Ty=%s '%str(Ty) + 'Lx=%s '%str(Lx) ...
+ 'Ly=%s '%str(Ly) + 'f0=%s '%str(f0)
plt.savefig('%s 3.png' %flag)

fig = plt.figure(figsize=(8,3), dpi=100)
ax = fig.gca()

cont = plt.contourf(X,Y,u_both,100,cmap='jet')
plt.contour(X,Y,u_both, 10, colors='black', linewidths=0.5)
```

```
#plt.colorbar(cont,orientation='horizontal')
ax.set_aspect('equal')
plt.axis('off')
#plt.title('Numerical Solution - Cross sectional view')
#ax.set_xlabel('x'), ax.set_ylabel('y')

flag='D=%s '%str(D) + 'Tx=%s '%str(Tx) + 'Ty=%s '%str(Ty) + 'Lx=%s '%str(Lx) ...
+ 'Ly=%s '%str(Ly) + 'f0=%s '%str(f0)
plt.savefig('%s 2.png' %flag)

fig = plt.figure(figsize=(7,7), dpi=100)
ax = fig.gca(projection='3d')

ax.plot_surface(X,Y,u_both)
#ax.set_aspect('equal')
plt.title('Numerical Solution')
ax.set_xlabel('x'), ax.set_ylabel('y'), ax.set_zlabel('u')
```

A.3 Experimental data processing code

A.3.1 Ballpark calculation for experimental setup

```
a = 50e-6; % [meter] half-height of channel
W = 1000e-6; % [meter] full width of channel
b = W/2;
kappa = 5.7e-10; % [m^2/s] diffusivity of fluorescein

U = .001; % [m/s] average inflow velocity
%flowrate = 1.2700e-07;
flowrate = U*((2*a)*W*1000); % [liter/second] infusion rate
```

```
fprintf('Flow rate = %5.5f ul/min \n',flowrate*10^6*60) % [ul/min]Print flow rate

%U = flowrate/((2*a)*W*1000);
ta = (1/20)*(W^2)/kappa; % Diffusive time scale
fprintf('95 percent dispersivity at = %5.5f seconds \n',ta); % Print diffusive time scale

Pe = (U*2*a)/kappa; % Peclet number
fprintf('Pe = %5.5f\n',Pe)
Pe_term = (1/210)*Pe^2; % Peclet term from dutta, should have Pe_term>>1
fprintf('Pe_term = %5.5f >> 1\n',Pe_term) % Print Peclet term

% Reynolds
rho = 997;
mu = 8.9e-4;
Re = rho*U*a/mu;
fprintf('Re = %5.5f \n',Re) % Print Reynolds

syringe_flow_rate = flowrate*1e9*60; % [nanoliter/minute] flowrate

if flowrate > 4.16e-10 && flowrate < 4.16e-4 % check if syringe pump capable of flowrate
    fprintf('Good Flowrate \n')
else
    fprintf('Bad Flowrate \n')
end

Channel_Length = (ta)*U*100; % Estimate a sufficient channel length
fprintf('Channel Length = %2.3f cm \n', Channel_Length) % Print channel length
```

A.3.2 Deformed channel shape measurement

```
% Reference images for white field and dark field
%wf = input('\nHow many white field images?');
%df = input('\nHow many dark field images?');


[FileName,PathName] = uigetfile('\\files.brown.edu\research\ENG_Harris_Shared\glee59 ...
\Deformable channel\19.9.26\*.*','Select White field images','MultiSelect', 'on');
FullPath = strcat(PathName,FileName);
file_type = FullPath(end-2:end);


clear I_wf
if file_type == 'tif'
    FileName = cellstr(FileName);
    [m,n] = size(FileName);
    for i=1:n
        FullPath_i = char(FullPath(i));
        I_wf(:,:,i) = imread(FullPath_i);
    end
elseif file_type == 'avi'
    MOVIEfile = VideoReader(FullPath);
    if MOVIEfile.Duration == 1
        ref_frame.start = 1;
        ref_frame.end = 1;
    else
        implay(FullPath);
        ref_frame.start = input('\nStart Frame Number: ');
        ref_frame.end = input('\nEnd Frame Number: ');
    end
```

```
    for i = ref_frame.start:ref_frame.end
    i
    ref_I = double(read(MOVIEfile,i));
    I_wf(:,:,i-ref_frame.start+1)=ref_I;
    end
end

[FileName,PathName] = uigetfile('R:\glee59\Deformable channel/*.*', ...
'Select Dark field images','MultiSelect', 'on');
FileName = cellstr(FileName);
FullPath = strcat(PathName,FileName);
[p,q] = size(FileName);
clear I_df
for i=1:q
    FullPath_i = char(FullPath(i));
    I_df(:,:,i) = imread(FullPath_i);
end

mean_wf = mean(I_wf,3);
mean_df = mean(I_df,3);
factor = mean(mean(mean_wf-mean_df));


%% Select the region to crop

[FileName,PathName] = uigetfile('\\files.brown.edu\research\ENG_Harris_Shared\glee59 ...
\Deformable channel\19.10.3\*.*','Select Video to correct shading');
```

```
FullPath = strcat(PathName,FileName);
file_type = FullPath(end-2:end);

if file_type == 'avi'
    MOVIEfile = VideoReader(FullPath);
    fps = MOVIEfile.FrameRate;
    if MOVIEfile.Duration == 1
        frame.start = 1;
        frame.end = 1;
    else
       % implay(FullPath);
        frame.start = input('\nStart Frame Number: ');
        frame.end = input('\nEnd Frame Number: ');
    end
end

%frame.mid = round((frame.start+frame.end)/2);
% I = read(MOVIEfile,frame.mid);
% [~,RECT] = imcrop(I); %crop
pixels = 100;
RECT = [0.51,1944/2-pixels/2,2592,pixels];

%% Correcting uneven illumination

clear NewImag
if file_type == 'avi'
    for i = frame.start:frame.end
        i
```

```
        I = double(read(MOVIEfile,i));

        I = (I-mean_df)./(mean_wf-mean_df) * factor;

        I=imcrop(I,RECT);

        Ave_I = mean(I);

        NewImag(i-frame.start+1,:)=Ave_I;

    end

     NewImag = mean(NewImag); % Average the whole video


elseif file_type == 'tif'

    I = double(imread(char(FullPath)));

    %I = (I-mean_df)./(mean_wf-mean_df) * factor;

    I=imcrop(I,RECT);

    Ave_I = mean(I);

    NewImag = Ave_I;

end


scale = 4.61; % 4.61 pixel/um

figure(7)

hold on

[t,s] = size(I);

plot(linspace(0,s/scale,s),transpose(NewImag))

xlim([0 s/scale])

ylim([0 200])

xlabel('um')

ylabel('intensity')

 title('Acrylic chip - Air WIdth 0.5, Pressure gauge')

legend('0kPa','+40kPa','+80kPa')

grid on
```

```
box on

figure(8)
[~,RECT] = imcrop(uint8(NewImag)); %crop
Newcrop=imcrop(NewImag,RECT);
I_max = max(transpose(Newcrop));
plot(linspace(frame.start,frame.end/fps,frame.end-frame.start+1),I_max)
ylim([0 200])
xlabel('time (s)')
ylabel('Max Intensity')
grid on
title('Photo bleaching test')
fprintf('\nComplete\n')
```

A.3.3 Visualizing the change in intensity as Figrue 35 - 1

```
%% Load Files and Crop
PathName = uigetdir('\\\ENG_Harris_Shared\glee59\Deformable channel\19.11.17 ...
\-5kPa - 15cm +50s 1fps','Select Folder to Process')
AllFile = strcat(PathName,'/*.jpg');
Listing = dir(AllFile);
L = length(Listing);

FPS = 1;
RecordStart = 50;
x0 = 150;



mid = round(L/2);
```

```
midPath = strcat(PathName,'\',Listing(mid).name);
midI = imread(midPath);
[~,RECT] = imcrop(midI); %crop
%% Converting Video into conc Matrix
clear conc
for i=1:L
    iPath = strcat(PathName,'\',Listing(i).name);
    RGBCh=imread(iPath);% RGB Channel data
    BlueCh = RGBCh(:,:,3); % B Channel data only

    Inv_BlueCh = 255 - BlueCh; % Invert blue channel data

    I=imcrop(Inv_BlueCh,RECT);  % Crop
    mean_I = mean(I,2);
    conc(:,i) = mean_I;

    disp('Processing image #')
    disp(i)
end

close all



%% Selecting frame start and frame end to analyze
hold on
ave_conc = mean(conc);
plot(ave_conc)
```

```
grid on
xlabel('Frame')
ylabel('Averaged intensity of selected region')

%% Concentration over Time, calculation and plot
%frame.start = input('\nStart Frame Number: ');
%frame.end = input('\nEnd Frame Number: ');
frame.start=1;
frame.end=200;
close all

final_conc = ave_conc(1,frame.start:frame.end);

datastart = (frame.start-1)/FPS + RecordStart; % [seconds]
dataend = datastart + ((size(final_conc,2)-1)/FPS);

time = linspace(datastart, dataend, frame.end-frame.start+1);
% (start, start+duration, # frames)
hold on
plot(time,final_conc)
xlabel('Time [s]')
ylabel('Intensity')
grid on
xlim([datastart,dataend])

[~,expframemax] = max(final_conc);
exptmax = time(expframemax)
```

```
%% Normalize / Peak change
maxI = max(final_conc);
minI = min(final_conc);
N = (final_conc - minI) * 100/(maxI-minI);

tmax = 150;
T = time + (tmax - exptmax);

%% %%
close all
Normalize = (conc - minI) * 100/(maxI-minI);
Vis = uint8(Normalize);
imshow(Vis)

imwrite(Vis,'\\files.brown.edu\research\ENG_Harris_Shared\glee59 ...
\Deformable channel\19.11.17\Visualization\-3.tif')
```

A.3.4 Visualizing the change in intensity as Figrue 35 - 2

```
%%%%%% Python code %%%%%%
import matplotlib as mpl
import matplotlib.pyplot as plt
import matplotlib.image as mpimg
import numpy as np
from PIL import Image

cmap = mpl.cm.get_cmap('inferno')
img_src = Image.open(r'\\files.brown.edu\research\ENG_Harris_Shared\glee59 ...
\Deformable channel\19.11.17\Visualization\-3.tif').convert('L')
```

```
max = np.max(img_src)
min = np.min(img_src)
img_src = (img_src-min)/max*1
#img_src.thumbnail((512,512))
im = np.array(img_src)
im = cmap(im)
im = np.uint8(im * 255)
im = Image.fromarray(im)
display(im)
im.save(r'\\files.brown.edu\research\ENG_Harris_Shared\glee59\Deformable channel ...
\19.11.17\Visualization\Converted-3.tif')
```

A.3.5 Curvefitting function

```
function [fitresult, gof] = createFit1(time, final_conc)
%CREATEFIT1(TIME,FINAL_CONC)
%  Create a fit.
%
%  Data for 'untitled fit 1' fit:
%      X Input : time
%      Y Output: final_conc
%  Output:
%      fitresult : a fit object representing the fit.
%      gof : structure with goodness-of fit info.



%% Fit: 'untitled fit 1'.
[xData, yData] = prepareCurveData( time, final_conc );
```

```
% Set up fittype and options.
ft = fittype( '(C/sqrt(t))*exp((-(x0-0.001*t)^2)/(4*K*t))+h', ...
'independent', 't', 'dependent', 'y' );
opts = fitoptions( 'Method', 'NonlinearLeastSquares' );
opts.Display = 'Off';
opts.Lower = [0 0 0 0];
opts.StartPoint = [300 0 14 0.025];

% Fit model to data.
[fitresult, gof] = fit( xData, yData, ft, opts );

% Plot fit with data.
figure( 'Name', 'untitled fit 1' );
h = plot( fitresult, xData, yData );
legend( h, 'final_conc vs. time', 'untitled fit 1', 'Location', 'NorthEast' );
% Label axes
xlabel time
ylabel final_conc
grid on
```